INTERNATIONAL JOURNAL FOR NUMERICAL AND ANALYTICAL METHODS IN GEOMECHANICS
Int. J. Numer. Anal. Meth. Geomech. (2014)
Published online in Wiley Online Library (wileyonlinelibrary.com). DOI: 10.1002/nag.2294

Blast-induced rock fracture near a tunnel

Ling Xu[1,*,†], Howard Schreyer[2] and Deborah Sulsky[3,*]

[1]*Department of Mathematics and Statistics, Georgia State University, Atlanta, Georgia, U.S.A.*
[2]*Department of Mechanical Engineering, University of New Mexico, Albuquerque, New Mexico, U.S.A.*
[3]*Department of Mathematics and Statistics, Department of Mechanical Engineering, University of New Mexico, Albuquerque, New Mexico, U.S.A.*

SUMMARY

Damage in the form of cracks is predicted to assess the susceptibility of a tunnel to failure due to a blast. The material-point method is used in conjunction with a decohesive failure model as the basis for the numerical simulations. The assumption of a cylindrical charge as the source for the blast allows the restriction of plane strain and two-dimensional analyses. In the simulation, a further restriction of a single pressure pulse is used as the source of stress waves that are reflected and refracted after reaching the free surface of the tunnel wall. Three critical zones of significant cracking in the vicinity of a tunnel are identified as potential contributors to tunnel failure. Copyright © 2014 John Wiley & Sons, Ltd.

Received 30 August 2013; Revised 15 March 2014; Accepted 17 March 2014

KEY WORDS: blast wave simulation; material-point method; tunnel failure; decohesive model for rock failure

1. INTRODUCTION

Sources of strong ground motion include explosions and earthquakes. Explosions near structures can be more damaging than earthquakes because of the proximity and frequency content of the waves. Blasts can be intentional or accidental, and beneficial, as in rock quarrying, or malevolent, as in an attack. In any case, it is of interest to understand the impact of a blast on above-ground or below-ground structures in order to mitigate unintended damage, to protect critical structures or to design survivable structures. Variables such as the blast magnitude and site geology can affect the ground motion, and the geometry of the structure and its distance to the blast can influence the amount of damage. This paper examines fractures, induced by a blast, in rock surrounding a tunnel. The ultimate goal is a predictive numerical model that can provide stress wave intensities and predict damage to structures.

The complicated properties of both the rock and the explosive make the prospect of detailed computations daunting. Nevertheless, some work has been carried out toward this goal. Yang [1] models a shelter in soil subjected to blast loading. This two-dimensional finite element solution in Cartesian geometry uses a viscoelastic constitutive model for the soil. The detonation of the explosive is not explicitly modeled. Instead, the detonation is represented by a pressure load applied on the circumference of a circle whose center corresponds to the center of the explosive charge. A more realistic, three-dimensional finite element solution using a Cam-Clay model for the soil surrounding a tunnel is carried out in Ortiz and Pandolfi [2]. Wang *et al.* [3] merge smooth particle hydrodynamics (SPH) with the finite element method in a fully coupled approach to modeling the

*Correspondence to: L. Xu, Department of Mathematics and Statistics, Georgia State University, Atlanta, Georgia, U.S.A. and Deborah Sulsky, Department of Mathematics and Statistics, University of New Mexico, Albuquerque, New Mexico, U.S.A.
†E-mail: lxu9@gsu.edu; sulsky@math.unm.edu

detonation, wave propagation and structural response in a two-dimensional axisymmetric study of a subsurface blast near an underground structure. SPH is used to model the near-field response, and finite elements are used to model the intermediate and far-field ground movement, plus the structural response. A three-phase soil model [4] and the Riedel–Thoma–Hiermaier [5] concrete model are used for the soil and structure, respectively. The Jones–Wilkins–Lee (JWL) equation of state is adopted for simulating the detonation.

Hao *et al.* [6, 7] develop an anisotropic damage model to analyze granite under blast loads. The damage accumulates by degrading effective material stiffness and strength, and the model takes into account pre-existing cracks and joints in the rock. Three-dimensional simulations are carried out and compared with field tests for an explosive placed in a borehole in granite. The explosive (TNT) is modeled using the JWL equation of state. Similar analysis in later work [8, 9] models the effect of an underground blast on above-ground structures, and rock mass damage due to an explosion in an underground ammunition storage chamber [10].

Instead of a damage model, we model rock using a combination of elasticity and a decohesive failure model. The intent of the model is to predict the initiation, direction and evolution of fractures in the rock. The model is based on tensile failure with a modification to account for the effects of shear and axial splitting. Numerical simulations are performed in two dimensions using the material-point method (MPM). In this study, we assume that a tunnel is located in granite with representative properties. We exclude the details in the immediate vicinity of an explosive charge by prescribing a compressive pulse on a boundary of a blast zone at a radius beyond which primarily elastic-decohesive behavior is expected. The assumption of a cylindrical charge parallel to the tunnel allows us to invoke the two-dimensional restriction of plane strain. The combination of MPM and the elastic-decohesion constitutive equation has been used previously in large-scale simulations of failure in Arctic ice [11–13].

A blast from a cylindrical charge without a nearby tunnel has been studied by several authors. Banakaki and Mohanty [14] examine fracture patterns in cylindrical samples of granite explosively loaded in a central borehole. They compare laboratory experiments with numerical simulations using ANSYS AUTODYN and a Johnson–Holmquist (J–H) model for granite and the JWL model for the detonation. Zhu *et al.* [15] use the same code and compare the effects of four different equations of state to model the detonation, combined with a modified principal stress criterion used to predict failure in a diorite rock. The modified principal stress failure criterion dictates that when the major principal stress or the maximum shear stress in an element exceeds material tensile or shear strength, the element fails. Ma and An [16] use the J–H model in LS-DYNA to predict crack patterns, but with the blast modeled as an applied pressure pulse. Hamiel *et al.* [17] also study cylindrical granite specimens in order to develop an anisotropic constitutive model describing effective damaged material properties of granite. Khan [18] demonstrates that two-dimensional discrete element method can give varied fracture patterns in a disk loaded by a cylindrical tensile wave.

We choose to model the effect of the blast loading by prescribing a single pressure pulse on the boundary of a cylinder concentric with the center of the explosion. The simplification of a single pulse allows us to observe details of the wave propagation clearly. Section 2 specifies the details of the problem to be solved and specifies all of the simplifying assumptions. In Section 3, we introduce the decohesive failure model used to predict crack formation in the rock. The model includes the possibility of axial splitting, a mode of failure not normally included in failure models.

Representative values of material parameters for granite are given in Section 4.1. Because a pulse in cylindrical geometry changes shape when it propagates, we find it useful to present first the results of one-dimensional elastic-wave propagation assuming axisymmetry in Section 4.2. In considering the elastic waves, we examine both the free-field solution and the solution with reflected waves from a nearby tunnel. We use the terminology free-field or free-wave propagation to designate the situation if the tunnel is absent. These solutions provide the initial insight into features of wave propagation and potential failure modes in rock near a tunnel. In particular, the initial compressive pulse develops a trailing tensile phase as the cylindrical wave propagates away from the source. We call this effect a tensile tail. As the initial compressive pulse reflects off the free surface forming the

DOI: 10.1002/nag

tunnel wall, it can interact with the tensile tail, amplifying the effect of the reflected wave. The analysis continues in Sections 4.3 and 4.4 with two-dimensional simulations of elastic waves, with and without the tunnel, respectively.

Next, in Section 4.5, we show the free-field crack pattern, and then, we include the tunnel in the simulations in Section 4.6. The first important feature of note is that the tensile tail that evolves because of cylindrical wave propagation expands to the point where tensile failure may occur. This effect is magnified when the compressive part of the wave reflects off the free surface of a tunnel wall. The result is a significant fracture zone near the tunnel wall closest to the blast. If the blast pulse is sufficiently large, axial splitting may also occur at segments of the tunnel wall defined roughly by tangent lines from the source. Axial splitting parallel to a wall can result in spall and, consequently, the formation of rubble within a tunnel. These patterns suggest specific zones of potential damage along and near the tunnel wall and suggest points for detailed investigations. Section 5 provides these details in the form of plots of stress versus time at selected points.

In Sections 5.3 and 5.4, we vary the pulse duration and blast orientation. Two cases are considered: (i) short and long pulses applied to the side of the tunnel and (ii) an overhead explosion causing direct loading on the roof for two pulse durations. Section 5.5 briefly discusses the energetics of the failure process.

Finally, Section 6 summarizes our results. The features of tensile tails, enhancement due to reflection, and the possibility of axial splitting tangent to tunnel walls represent new features identified by this research. Damage in the form of a displacement discontinuity is stored and provides the basis for possible additional analyses of subsequent blast loading within a damaged medium. The decohesive model also allows more than one crack through a point, so branching and interacting cracks are possible.

2. PROBLEM DESCRIPTION AND SIMPLIFYING ASSUMPTIONS

The problem consists of an explosive charge detonated at some distance from a tunnel in a material with features representative of granite. The physical problem is three dimensional. However, for this study, our first assumption is that the blast source is cylindrical with the axis of the cylinder parallel to the centerline of the tunnel. Then the restriction of plane strain is appropriate provided that the normals to planes of fracture lie within the symmetry plane and the problem remains two dimensional.

The region of material immediately surrounding an explosive is subject to extreme pressure, high temperature, multiple fractures, high strain rates and large inelastic deformation. Modeling the explosive itself is a challenge, let alone the damage it causes. Therefore, our second simplifying assumption is to represent the effect of the explosive as a compressive pulse prescribed on the surface of a cylinder with a radius sufficiently large that the response of the material beyond this radius is primarily elastic with cracking. A sketch of the domain indicating this simplification is shown in Figure 1. In the following, any mention of a cylinder refers to the explosive charge, modeled as a stress pulse on the interior of the cylindrical cavity, taken to be of radius 3 m.

Assumption three is an idealized tunnel geometry described by a roof consisting of a circular arc supported by rectangular sides and a bottom, each of length 6 m. The radius of the roof is 3 m. This geometry is also sketched in Figure 1.

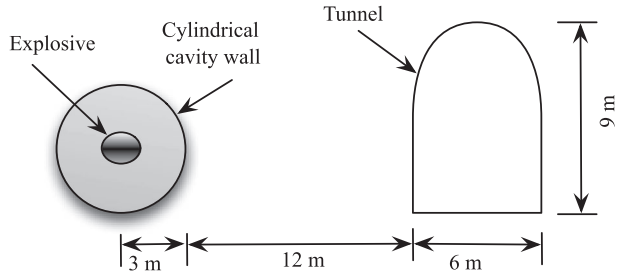

Figure 1. Geometry of the explosive, equivalent cylindrical cavity and tunnel.

DOI: 10.1002/nag

The fourth assumption is that the effect of the explosion can be modeled by a forcing function on the surface of the cylinder as a single compressive pulse of finite duration and a magnitude that provides a reasonable particle velocity for a point 3 m from the center of the charge as suggested by experimental data. The prescribed pressure on the surface of the cylinder is a single smooth cosine pulse whose duration is denoted by t_D and whose amplitude is σ_0. Specifically, the form is

$$\sigma_{rr}(t)|_{r=3\mathrm{m}} = -\frac{\sigma_0}{2}[1 - cos(2\pi t/t_D)]H[t]H[t_D - t] \tag{1}$$

in which $H[t]$ denotes the Heaviside function. As it turns out, the great value of this assumption is that key features can be identified in the stress wave transmitted to and reflected off the tunnel, features that might not be obvious if a more complex, and presumably a more realistic, forcing function was used.

Our fifth assumption is that the rock medium beyond the cylinder can be modeled with a combination of isotropic elasticity and cohesive failure with the effect of the latter spread over an element and represented by smeared crack strains. In reality, some plastic deformation is expected to occur, but the related energy dissipation is expected to be small in comparison with the dissipation associated with fracture. Within a limited range of stress, material failure is assumed to be brittle in the sense that the normal to the failure plane is in the direction of maximum principal stress and failure opening is mode I; that is, the displacement discontinuity is in the direction of the normal. However, outside this limited domain of stress, the failure function allows for the prediction of axial splitting under uniaxial compression and of mixed-mode failure under triaxial compression.

Finally, the last assumption is that the blast occurs close to the tunnel as compared with its depth below ground so that it is not necessary to consider reflected waves from the ground surface. The size of the computational domain can be chosen so that results in the vicinity of the tunnel are not affected by reflections from the computational domain boundary and non-reflective boundary conditions are not necessary. The computational domain with the tunnel is shown in Figure 2(a). Figure 2(b) is an enlargement of Figure 2(a) in the vicinity of the cylindrical source with observation points identified for the analysis to follow.

3. DECOHESIVE FAILURE MODEL

3.1. The model

The decohesive model used to predict failure has been used previously to study the formation of leads in Arctic ice under the assumption of plane stress [11]. Here, we investigate a problem under plane strain rather than plane stress, so a three-dimensional version of the model is necessary. Because

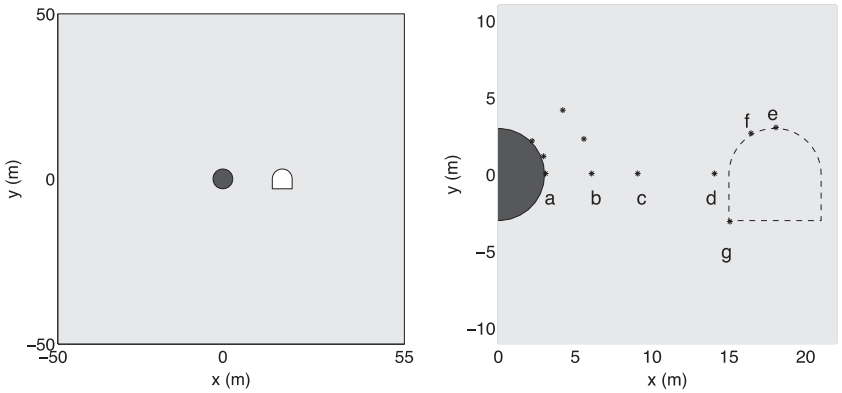

(a) Domain with source and tunnel (b) Enlargement and observation points.

Figure 2. The computational domain of $-50\,\mathrm{m} < x < 55\,\mathrm{m}$ and $-50\,\mathrm{m} < x < 50\,\mathrm{m}$ showing the location of source, tunnel and observation points for displaying stress histories.

DOI: 10.1002/nag

some features of the failure surface in stress space are slightly different than the previous formulation, a summary of the model is presented.

Consider a potential surface of material failure identified with normal $\boldsymbol{n}$. Introduce an orthonormal triad ($\boldsymbol{n}$, $\boldsymbol{t}$, $\boldsymbol{p}$) so that the tangent plane to the material failure surface is the $\mathbf{t}-\mathbf{p}$ plane. The traction on the material failure surface is

$$\tau = \tau_n \boldsymbol{n} + \tau_t \boldsymbol{t} + \tau_p \boldsymbol{p} \tag{2}$$

If failure is occurring, then the corresponding displacement discontinuity is

$$[\boldsymbol{u}] = [u_n]\boldsymbol{n} + [u_t]\boldsymbol{t} + [u_p]\boldsymbol{p} \tag{3}$$

The possibility of initial failure, or continuing failure, is indicated by a failure decohesive function $F_n(\boldsymbol{\tau}, \{\sigma^\circ\}, f_n)$ constructed such that $F_n < 0$ implies that failure evolution is not occurring, $F_n = 0$ indicates that failure evolution is possible and $F_n < 0$ is not allowed. Let $\boldsymbol{\sigma}$ denote the stress tensor. The set $\{\sigma^\circ\}$ denotes other components of stress not contained within $\boldsymbol{\tau}$ and allows the capability for predicting axial splitting and separates the proposed model from classical formulations such as the Rankine, Tresca and Mohr–Coulomb models. The softening function, f_n, provides the current state of failure where $\overline{u}$ is a scalar measure of the development of failure, or effective decohesion. For convenience, the function is chosen to be $f_n = 1 - \overline{u}$. The angle brackets denote the ramp function $\langle x \rangle = x$ if $x > 0$, otherwise $\langle x \rangle = 0$, so that $f_n = 0$ if $\overline{u} \geq 1$. The linear softening relation is assumed for convenience. If $f_n = 1$ $(\overline{u} = 0)$, then failure has not initiated; if $1 > f_n > 0$ $(0 < \overline{u} < 1)$, then a microcrack has developed; and finally, if $f_n = 0$ $(\overline{u} \geq 1)$, then the microcrack has evolved to a macrocrack or, equivalently, to a crack, with the formation of two new free surfaces.

Prior to the formation of a microcrack, all orientations for $\boldsymbol{n}$ must be considered, and the worst case is used to identify a specific choice for $\boldsymbol{n}$. To this end, define a general decohesive function as follows:

$$F = \max_{\substack{all \\ \boldsymbol{n}}} F_n \tag{4}$$

During a loading scenario for a given problem, all material points must be checked continuously for the possibility of failure initiation. With numerical procedures, these points are finite in number and explicitly defined. If $F < 0$, then the failure condition is not satisfied, and the continuum constitutive equation holds for that point. A crack is initiated once $F = 0$. In a numerical procedure for this material point, storage is allocated for the components of $\boldsymbol{n}$, the components of the displacement discontinuity, and the effective decohesion, $\overline{u}$. There may be more than one material failure surface at any one material point.

For subsequent times in the loading scenario, those points without failure are checked as before. For the points with a previously defined microcrack or macrocrack, the failure function for that orientation is checked to see if $F_n > 0$, which indicates that the existing crack must evolve to enforce the condition that $F_n = 0$. Then other orientations are considered to see if an additional failure surface with a different orientation is created for the same material point. If an additional surface is created, then storage must be allocated for the corresponding variables, just as they were for the first crack. Typically, we require the orientation of a new crack to be at least 5° different from previous ones and limit the number of cracks to be two or three.

The evolution equations related to decohesion are the following:

$$\begin{aligned} [\dot{\boldsymbol{u}}] &= \dot{\omega} \frac{\partial F_n}{\partial \boldsymbol{\tau}} \\ \dot{\overline{u}} &= \dot{\omega} \overline{m} \\ \dot{F}_n &= 0 \end{aligned} \tag{5}$$

in which ω is a monotonically increasing parameter introduced for convenience to parameterize the equations and $\overline{m}$ is an evolution function that is not specified for the moment.

DOI: 10.1002/nag

The decohesion function used for this study is the following:

$$F_n = \frac{\tau_s^2}{\left(s_m \tau_{sf}\right)^2} + e^{\kappa B_n} - 1 \qquad B_n = \frac{\tau_n}{\tau_{nf}} + \frac{\sigma_{ec}^2}{\left(f_c^{'}\right)^2} - f_n \tag{6}$$

where the resultant shear traction is

$$\tau_s = \left(\tau_t^2 + \tau_p^2\right)^{1/2} \tag{7}$$

and σ_{ec} is an effective compressive stress that depends on the stress components $\{\sigma^{\circ}\}$. The effective compressive stress used in the simulations for this paper is $\sigma_{ec} = \ < -\sigma_{tt} >$ with σ_{tt} denoting the in-plane normal component of stress. In addition, τ_{nf} is the failure stress under uniaxial tensile stress, $f_c^{'}$ is the failure stress for uniaxial compression of a brittle material, and τ_{sf} is the failure stress under pure shear. A physical interpretation of the remaining material parameter, s_m, is discussed later. We will also see that the exponent, κ, is not independent but depends on the material parameter, s_m.

To illustrate the implications of the various terms in the failure function, we consider various scenarios with $f_n = 1$. First, suppose $\tau_s = 0$. Then $F_n = 0$ if $B_n = 0$ or

$$\frac{\tau_n}{\tau_{nf}} + \frac{\sigma_{ec}^2}{\left(f_c^{'}\right)^2} - 1 = 0 \tag{8}$$

The Rankine form for failure is obtained if $\sigma_{ec} = 0$, and failure occurs if $\tau_n = \tau_{nf}$. On the other hand, if $\tau_n = 0$, (8) implies that axial splitting is initiated if $\sigma_{ec} = f_c^{'}$.

Next, define the case of pure shear as the combination of values for τ_n and σ_{ec} in (6) that result in $B_n = -1$. We select κ to satisfy the following:

$$e^{-\kappa} - 1 = \frac{1}{s_m^2} \quad or \quad \kappa = ln\left[\frac{s_m^2}{s_m^2 - 1}\right] \tag{9}$$

Then, from (6), $F_n = 0$ implies that failure is initiated in shear when $\tau_t = \tau_{sf}$.

Next, suppose that two free surfaces have been formed so that $f_n = 0$. The condition $F_n = 0$ becomes

$$\frac{\tau_s^2}{\left(s_m \tau_{sf}\right)^2} + e^{\kappa B_n} - 1 = 0 \qquad \mathrm{B}_n = \frac{\tau_n}{\tau_{nf}} + \frac{\sigma_{ec}^2}{\left(f_c^{'}\right)^2} \tag{10}$$

Because failure has occurred, (10) is an implied frictional sliding equation after a macrocrack has developed. If $F_n < 0$ ($f_n = 0$), then slip is not occurring.

Now suppose that τ_n is large and negative so that $B_n \to -\infty$. Then, from (6),

$$F_n = \frac{\tau_s^2}{\left(s_m \tau_{sf}\right)^2} - 1 \quad B_n \to -\infty \tag{11}$$

Failure ($F_n = 0$) occurs if

$$\tau_s^2 = \left(s_m \tau_{sf}\right)^2 \tag{12}$$

irrespective of the value of f_n. This equation provides an interpretation of the parameter, s_m, namely the magnification of the shear failure strength for a material under large negative normal traction in comparison with the value for shear failure strength under pure shear.

DOI: 10.1002/nag

Next, consider the evolution equations for the displacement discontinuity from (5)

$$\begin{aligned}[\dot{u}_n] &= \dot{\omega}\frac{\partial F_n}{\partial \tau_n} = \dot{\omega}\frac{\kappa e^{\kappa B_n}}{\tau_{nf}} \\ [\dot{u}_s] &= \dot{\omega}\frac{\partial F_n}{\partial \tau_s} = \dot{\omega}\frac{2\tau_s}{\left(s_m \tau_{sf}\right)^2}\end{aligned} \tag{13}$$

in which

$$[\dot{u}_s] = \left\{[\dot{u}_t]^2 + [\dot{u}_p]^2\right\}^{1/2} \tag{14}$$

Note that $[\dot{u}_s]$ is nonzero only if τ_s is nonzero. On the other hand, $[\dot{u}_n]$ is positive even if τ_n is zero or negative. This is a consequence of assuming that B_n in expression (6) depends linearly on τ_n. It is often observed that a crack dilates under shear even if the normal component of traction is negative. Because of this property, it is believed that a suitable choice for the evolution equation of the effective displacement discontinuity is

$$\dot{\overline{u}} = \frac{[\dot{u}_n]}{[u_0]} \tag{15}$$

where $[u_0]$ is the value of the normal component of the displacement jump when a complete crack is formed under uniaxial tension. This assumption is certainly not valid for cases where a significant amount of shear occurs, but for our application, there is little or no shearing on failure planes. It follows from (5) and (15) that

$$\overline{m} = \frac{\partial F_n/\partial \tau_n}{[u_0]} \tag{16}$$

The failure energy is defined to be

$$W_F = \int \{\tau_n [\dot{u}_n] + \tau_s [\dot{u}_s]\} dt \tag{17}$$

By combining the two equations in (13) to eliminate $\dot{\omega}$, we obtain

$$[\dot{u}_s] = [\dot{u}_n]\frac{\tau_{nf}}{\kappa e^{\kappa B_n}}\frac{2\tau_s}{\left(s_m \tau_{sf}\right)^2} \tag{18}$$

so that (17) becomes

$$W_F = \int_0^{[u_0]} \left\{\tau_n + \frac{\tau_{nf}}{\kappa e^{\kappa B_n}}\frac{2\tau_s^2}{\left(s_m \tau_{sf}\right)^2}\right\}[du_n] \tag{19}$$

For uniaxial stress, $\tau_s = 0$ and the decohesive condition yields $\tau_n = \tau_{nf}(1 - [u_n]/[u_0])$. Then, (19) becomes

$$W_F = \frac{1}{2}\tau_{nf}[u_0] \tag{20}$$

If the mode I fracture energy W_{F1} and τ_{nf} are known for a material, then (20) is used to evaluate $[u_0]$. If shear is present, the fracture energy will be larger as indicated by (19).

DOI: 10.1002/nag

Introduce principal axes of stress ($\boldsymbol{e}_{max}, \boldsymbol{e}_{min}, \boldsymbol{e}_{int}$) associated with the maximum, minimum and intermediate principal values ($\sigma_{max}, \sigma_{min}, \sigma_{int}$). The result of numerical simulations for a large number of paths suggests that $\boldsymbol{n}$ lies in the plane of maximum and minimum principal stress. This result appears to be substantiated by experimental data for a number of materials. Because we do not have proof that this should always be the case, we make the assumption that $\boldsymbol{n}$ lies in the ($\boldsymbol{e}_{max} - \boldsymbol{e}_{min}$) plane. If $\boldsymbol{t}$ is chosen to lie in this plane, then the orientation of $\boldsymbol{n}$ is simply described by a single angle, θ_n, between $\boldsymbol{n}$ and $\boldsymbol{e}_{max}$ so that

$$\mathbf{n} = \cos\theta_n \mathbf{e}_{\max} + \sin\theta_n \mathbf{e}_{\min} \tag{21}$$

With this simplification, we note that $\tau_s = \tau_t$. Furthermore, because $\sigma_{tp} = 0$, let us define the square of the effective compressive stress to be a quadratic combination of σ_{tt} and σ_{int} as follows:

$$\sigma_{ec}^2 = <-\sigma_{tt}><-\sigma_{tt}> + C_1 <-\sigma_{tt}><-\sigma_{int}> + C_2 <-\sigma_{int}><-\sigma_{int}> \tag{22}$$

in which C_1 and C_2 are material constants. It follows that both components σ_{tt} and σ_{int} contribute to the value of σ_{ec} if each is negative. The material constants C_1 and C_2 must be chosen to render the right-hand side of (22) positive.

Under uniaxial compression, $\boldsymbol{t} = \boldsymbol{e}_{min}$, and $\sigma_{ec} = <-\sigma_{tt}>$. For mode I failure ($\sigma_{int} = \sigma_{max} = 0$) and $\sigma_{tt} = -f_c^{'}$, $\sigma_{min} = \sigma_{int}$ and $\sigma_{max} = 0$. Next, suppose that $f_b^{'}$ is the failure stress under equal biaxial compression so that $\sigma_{\min} = \sigma_{\text{int}} = -f_b^{'}$ and $\sigma_{\max} = 0$. Under the assumption of mode I failure, $\sigma_{ec}^2 / f_c^{'} 2 = 1$, or

$$C_1 = \frac{f_c^{'2}}{f_b^{'2}} - 1 - C_2 \tag{23}$$

If $f_b^{'} = 1.2 f_c^{'}$ and $C_2 = 1$, then $C_1 = -1.31$. On the other hand, if $f_b^{'} = f_c^{'}$ and $C_2 = 0$, then $C_1 = 0$, and $\sigma_{ec} = <-\sigma_{tt}>$. This latter choice of $f_b^{'}$ and C_2 removes any contribution of the intermediate principal stress to the effective compressive stress.

3.2. *Procedure for finding the critical orientation*

The search for the critical orientation of the failure surface in physical space is not as daunting as it might seem. With $\gamma = sin^2\theta_n$, the transformation relations yield

$$\begin{aligned} \tau_n &= \sigma_{max}(1-\gamma) + \sigma_{min}\gamma \\ \sigma_{tt} &= \sigma_{max}\gamma + \sigma_{min}(1-\gamma) \\ \tau_t^2 &= (\sigma_{min} - \sigma_{max})^2 \gamma(1-\gamma) \end{aligned} \tag{24}$$

Substitute (24) in (6), and set

$$G \equiv \frac{\partial F_n}{\partial \gamma} = 0 \tag{25}$$

The object is to find the value of γ and, hence, θ_n, which renders F_n a maximum. We note that

$$\frac{\partial F_n}{\partial \gamma} = \frac{1}{\left(s_m \tau_{sf}\right)^2} \frac{\partial}{\partial \gamma}\left(\tau_t^2\right) + \kappa e^{\kappa B_n} \frac{\partial B_n}{\partial \gamma} \tag{26}$$

and

DOI: 10.1002/nag

$$\begin{aligned}
\frac{\partial \tau_t^2}{\partial \gamma} &= (\sigma_{max} - \sigma_{min})^2(1 - 2\gamma) \\
\frac{\partial \tau_n}{\partial \gamma} &= -(\sigma_{max} - \sigma_{min}) \\
\frac{\partial \sigma_{tt}}{\partial \gamma} &= (\sigma_{max} - \sigma_{min}) \\
\frac{\partial \sigma_{ec}^2}{\partial \gamma} &= -H[-\sigma_{tt}](\sigma_{max} - \sigma_{min})\{2 < -\sigma_{tt} > + C_1 < -\sigma_{int} >\}
\end{aligned} \tag{27}$$

The result is

$$\frac{\partial B_n}{\partial \gamma} = -(\sigma_{max} - \sigma_{min})\left[\frac{1}{\tau_{nf}} + \frac{H[-\sigma_{tt}]}{\left(f_c^{'}\right)^2}\{2 < -\sigma_{tt} > + C_1 < -\sigma_{int} >\}\right] \tag{28}$$

By plotting F_n as a function of γ for several cases, it is seen that if $\partial F_n/\partial\gamma|_{\gamma=0} < 0$, (25) is not satisfied, and the maximum occurs at $\gamma = 0$. Therefore, it is most efficient to assume initially that the maximum occurs at $\gamma = 0$. The process needs to be extended to the case of (25) only if $\partial F_n/\partial\gamma|_{\gamma=0} > 0$. A Newton–Raphson procedure can be used to find the zero of G in which case the derivative $\partial G/\partial\gamma$ is required. These details are relatively straightforward and not included for the sake of brevity.

The two cases for finding the critical orientation are illustrated in Figure 3 for the specific case of uniaxial compression with $\sigma_{min} = -0.9 f_c^{'}$ and material parameters $\tau_{nf} = 1,\ f_c^{'} = 10,\ f_b^{'} = 10,\ s_m = 4,$ $C_2 = 0$. For the case of $\tau_{sf} = 4$, the dotted line is obtained, and the maximum of F_n occurs at $\gamma = 0$. When the shear failure term is reduced to $\tau_{sf} = 2$, the result is the solid line, and the maximum occurs at $\gamma = \gamma_M$ with the implication that failure evolution is a mixed mode.

Once γ_M is obtained, there are two solutions for the critical angle:

$$\theta_n = \pm \sin^{-1}\left(\sqrt{\gamma_M}\right) \tag{29}$$

When used in an actual numerical simulation, the sign is chosen so that the rotation implied by shear on a failure plane agrees with the sign of rotation for the element in which failure is occurring [13].

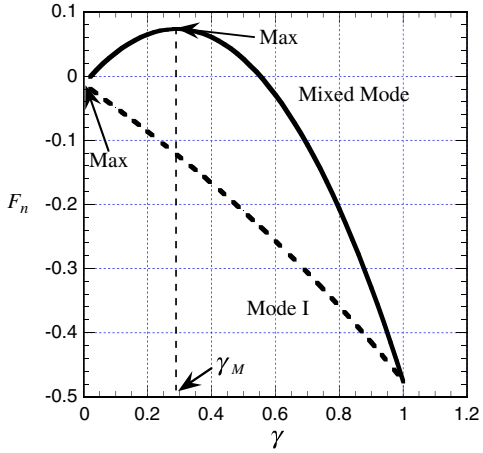

Figure 3. Representative plots of decohesion function as a function of γ with $\tau_{sf} = 2$ and $\tau_{sf} = 4$ denoted by the solid and dotted lines, respectively.

DOI: 10.1002/nag

3.3. *Features of the model*

With a suitable choice of parameters, the proposed model can match experimental data for the stress at which failure occurs and the mode of failure. For example, under the assumption of mode I failure, the experimental curves for failure of concrete under plane stress [19] can be reproduced. More significantly, the model can replicate the features exhibited by concrete and rock subjected to triaxial compression [20] where the mode of failure changes from axial splitting for uniaxial compression to mixed-mode failure with increasing shear contributions as the lateral pressure is increased. These features have been illustrated using a similar formulation for a failure function in [21] and are not repeated here.

Because the problem of interest is one of plane strain and because elasticity is assumed to hold up to the initiation of failure, it follows that $\sigma_3 = \nu(\sigma_1 + \sigma_2)$. A plot of the failure surface at initial failure is shown in the space of maximum and minimum principal stresses in Figure 4 for plane strain. The values chosen for material parameters are ($E = 10^4 \tau_{nf}, \nu = 0.21$) and $\left(\tau_{nf} = 1, \tau_{sf} = 4, f_c^{'} = 10, f_b^{'} = 10, s_m = 4, C_2 = 0\right)$, for the elasticity and failure models, respectively. All stress components are normalized with respect to τ_{nf}. Regions associated with specific pairs of maximum and minimum principal stresses are shown on the plot. Recall that the normal to the material failure surface is assumed to lie in the plane of eigenvectors associated with maximum and minimum principal stresses, and the angle between the normal and the eigenvector associated with the maximum principal stress is θ. Note that there is a rather sharp transition to a significant mixed-mode failure as indicated by θ changing from zero to 32° as either principal stress varies from -10 to -15. For much larger and negative minimum principal stresses, the failure mode comes close to $\theta = 45°$, the Tresca criterion. The failure surface in the upper right quadrants is similar to that for plane stress, and the main difference occurs when both principal stresses are negative. Figure 4(b) shows an abbreviated part of Figure 4(a) to highlight the range of stresses observed at points of interest for the tunnel problem. For some points, both the maximum and minimum principal stresses are positive (segment A-B). If these components happen to be equal, then there is an indeterminacy concerning the direction of $\boldsymbol{n}$ with the result that cracks at various orientations may form. The large majority of situations consist of different signs for the maximum and minimum principal stresses (segment B-C) in which case the normal vector is the eigenvector for maximum principal stress. In this work, negative values for both the maximum and minimum principal stresses (segment C-D) occur near the corner of the tunnel. For this regime, the normal changes value rather quickly with increases in the magnitude of minimum principal stress, and there is a high probability of mixed-mode failure.

The Rankine (maximum stress) criterion for failure initiation is shown as a dashed line in Figure 4 (b). Although the difference between the two criteria may appear small, we believe the possibility of axial splitting and mixed-mode failure in the regime C-D as opposed to no failure under

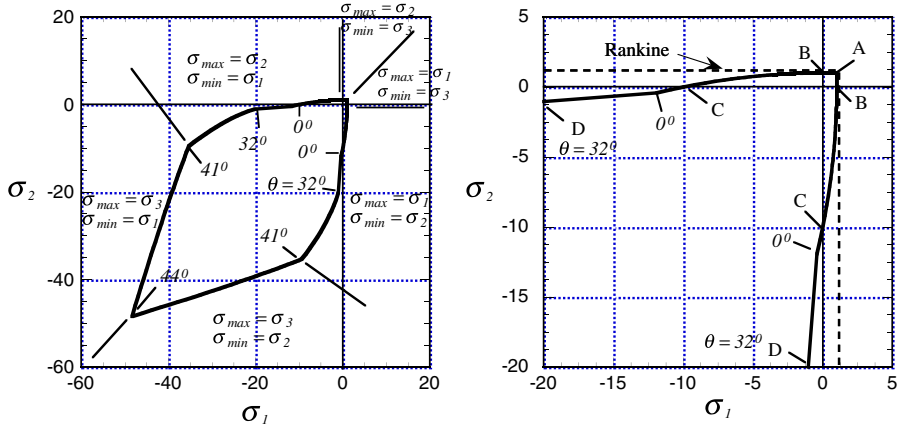

(a) Complete failure surface. (b) Expanded view near origin.

Figure 4. Plot of failure surface for principal stresses in the $\sigma_1 - \sigma_2$ plane under the condition of plane strain ($e_{33} = 0$).

DOI: 10.1002/nag

compressive stress for the Rankine criterion is a significant aspect not predicted with other existing decohesive failure models.

3.4. Critical element size

The displacement discontinuities obtained from the model of decohesion described in this section are used to obtain smeared crack-strain components in conjunction with the MPM. The procedure is described fully in Schreyer *et al.* [11] and is not repeated here. The crack strains produce a stress-softening feature within the element. If the element is larger than a critical size, there is a stress reversal, which cannot be handled without a major (undetermined) modification to the numerical procedure. If square elements of side h are used, stress reversal does not occur if h is less than a critical length h_{cr} where

$$h_{cr} \approx [u_0] \frac{E}{\tau_{nf}} \tag{30}$$

An element size somewhat smaller than the critical size is used to preclude reversal for all paths. The critical element size for mode I failure, which is typically the governing case, can be expressed in terms of the fracture energy with the use of (20)

The form of the decohesive model used here is satisfactory for relatively small magnitudes of stress. Large tensile stresses are limited by the value of τ_{nf}. In compression, agreement with features of experimental data for failure under triaxial compression (not shown) appears good at least for $\sigma_{\min} > -1.5f_c^{'}$, an inequality satisfied by all principal stresses obtained for this study. Experimental data on stress and orientation of failure surfaces must be used to select appropriate values for material parameters for a specific material.

4. GENERIC FEATURES OF ELASTIC AND ELASTIC-DECOHESIVE NUMERICAL SOLUTIONS

4.1. Elasticity and values of material parameters

Under plane strain, the nonzero components of strain are (e_{xx}, e_{yy}, e_{xy}), and the isotropic elastic constitutive relation for the nonzero stress components is

$$\begin{aligned} \sigma_{xx} &= E_1 e_{xx} + E_2 e_{yy} \qquad \sigma_{yy} = E_1 e_{yy} + E_2 e_{xx} \\ \sigma_{zz} &= E_2 \left(e_{xx} + e_{yy} \right) \qquad \sigma_{xy} = 2G e_{xy} \end{aligned} \tag{31}$$

where

$$E_1 = \frac{E(1-v)}{(1+v)(1-2v)} \qquad E_2 = \frac{E_1 v}{(1-v)} \qquad 2G = \frac{E}{(1+v)} \tag{32}$$

and E and v denote Young's modulus and Poisson's ratio, respectively.

In this section, solutions are presented for the case where the decohesive model of Section 3 is combined with isotropic elasticity. The value for τ_{sf} is chosen to enforce the assumed restriction that failure for granite should always be mode I under plane stress. However, mixed-mode failure is still possible for plane strain. For the sake of computational efficiency, the effect of the intermediate principal stress is excluded by choosing $f_b^{'} = f_c^{'}$ and $C_2 = 0$. As will be seen, failure under biaxial compression can exist at the lower corner of the tunnel, but the magnitude of one compressive principal stress remains small, so the simplification should not introduce significant error. The remainder of the values for the failure material parameters used in the numerical simulations is given in Table I.

DOI: 10.1002/nag

Table I. Material properties.

Elastic and mass properties		Failure properties	
Young's modulus	$E = 50\,\text{GPa}$	Tensile strength	$\tau_{nf} = 5\,\text{MPa}$
Poisson's ratio	$\nu = 0.21$	Compressive strength	$f'_c = 50\,\text{MPa}$
		Shear strength	$\tau_{sf} = 20\,\text{MPa}$
Mass density	$\rho = 2660\,\text{kg/m}^3$	Shear magnification	$s_m = 4$
		Exponent	$\kappa = 0.0645$
		Cohesive length	$u_0 = 3 \times 10^{-5}\,\text{m}$

The critical stress intensity factor for granite is assumed to be roughly twice that of concrete, or $K_c = 2$ MPa $\text{m}^{1/2}$, and the corresponding fracture energy is $G_f = K_c^2/E = 80$ Pa m. For the linear softening relation assumed for decohesion, the value of the parameter $[u_0]$ denoting complete failure becomes $[u_0] = 2G_f/\tau_{nf} = 3 \times 10^{-5}$m. The magnitude of the prescribed forcing pulse (1) is $\sigma_0 = f'_c$. Under the assumption of uniaxial stress, the corresponding maximum particle velocity at the surface of the cavity is $v_{\max} = \sigma_0/\sqrt{\rho E} = 4.3$ m/s. The pulse duration is $t_D = 3$ ms unless specified otherwise.

4.2. *One-dimensional elastic-wave analysis*

For the non-specialist in wave propagation theory, the evolution of cylindrical waves with time and the effects of reflections off free surfaces are sufficiently complex to warrant an initial one-dimensional analysis. Furthermore, one-dimensional results provide insight into the potential fracture patterns that may be initiated. The one-dimensional analysis also makes obvious the additional ramifications provided by a two-dimensional analysis that can be properly attributed to non-axisymmetric features due to reflection, refraction and fracture. One-dimensional results from a separate numerical code also serve as partial verification of the two-dimensional numerical procedure.

The model problem we consider consists of a cylindrical cavity and a pressure pulse prescribed on the surface. For sufficiently short time and elastic behavior, the problem is axisymmetric, so a one-dimensional analysis in cylindrical coordinates (r, θ) under the assumption of plane strain is appropriate.

In one dimension, the governing equation of motion is

$$\frac{1}{r}(r\sigma_{rr})_{,r} - \frac{\sigma_{\theta\theta}}{r} = \rho a \tag{33}$$

in which a comma denotes a derivative with respect to r, the radial coordinate; a denotes the radial acceleration; and σ_{rr} and $\sigma_{\theta\theta}$ denote the normal components of stress in the radial and circumferential directions, respectively. If u denotes the radial displacement, the radial and circumferential components of strain are $e_{rr} = u_{,r}$ and $e_{\theta\theta} = u/r$, respectively. The elastic constitutive equations under plane strain are analogous to those given in (31).

The domain is $r_0 \le r \le r_1$. The boundary condition at $r_0 = 3$ m is given by (1). A free-field solution is obtained by choosing a large value for r_1; for the time period of interest, $r_1 = 39$ m is adequate to avoid reflections from this boundary. To illustrate the effect of reflection off a free surface, $r_1 = 15$ m is used.

The numerical solutions for the one-dimensional case are based on the finite element method with explicit time integration and a time step of $0.5h/c_w$, where the wave speed is approximately $c_w \approx \sqrt{E_1/\rho} = 4600$ m/s. A convergence study indicates that an element size of $h = 0.25$ m is satisfactory. From (30), the critical element size is $h_{cr} = 0.3$ m. The element size $h = 0.25$ m meets this 'stability' criterion.

The free-field solutions for stress and velocity as functions of time are given in Figure 5 at the designated radial positions. With regard to the radial stress, we note that the stress in the first element reflects the forcing function, as it should. For increasing values of r, the stress profiles are typical of cylindrical waves in that a tensile tail is exhibited. The magnitude of the compressive phase decreases rapidly whereas the magnitude of the tensile phase evolves to a maximum of

DOI: 10.1002/nag

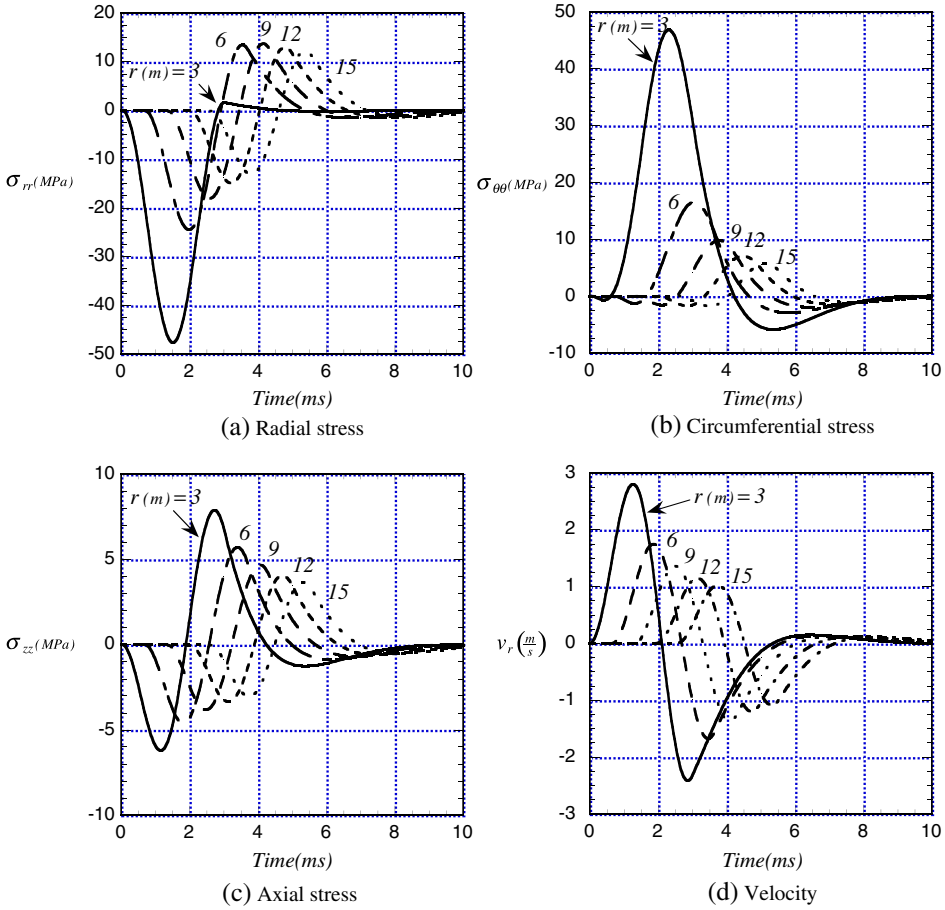

Figure 5. Plots of free-field stress and velocity as functions of time at the designated locations for the one-dimensional elastic case.

approximately 14 MPa and then decays. Note that this maximum is significantly greater than the assumed tensile strength τ_{nf} (Table I) so we see immediately that circumferential cracking for $r > 3$ m is possible, a feature that would not exist for uniaxial or planar waves. If the magnitude of the forcing pulse is reduced sufficiently, then circumferential cracking will not occur.

A slightly different situation, but with a change of sign, exists for the circumferential stress. This component begins with a large tensile phase and a compressive tail immediately at $r = 3$ m. The magnitudes of both the tensile and compressive parts decrease rapidly with increasing r. An important observation is that the presence of large positive values of stress for small r suggests that radial cracking can be expected to extend from the cylindrical wall to interior points.

The axial stress (z-direction) and the velocity profiles are provided for general information. Note immediately that there is a possibility of tensile failure with normal in the z-direction. If such a failure occurs, then the assumption of plane strain is violated, and the use of a two-dimensional analysis cannot be justified. However, if circumferential failure is allowed, then it will be seen that the axial component of stress will not achieve a value sufficiently large to cause failure. The velocity plot shows that the maximum value of radial velocity, 2.8 m/s at $r = 3$ m, is considerably smaller than the 4.3 m/s estimated for uniaxial stress.

Next, we consider the case of a free surface at $r = 15$ m as a one-dimensional representation of the tunnel wall. Plots of radial and circumferential stress at $r = 9$, 12 and 15 m are shown in Figure 6. The time for a wave to travel from the cavity wall to the free surface is about 2.6 ms. The time for the front of the stress wave to travel to the tunnel, back to the cylinder, and then from the cylinder surface to $r = 9$ m, is approximately 7 ms. Therefore, the duration of the plots is limited to this time to exclude extraneous reflections off the cylinder wall.

DOI: 10.1002/nag

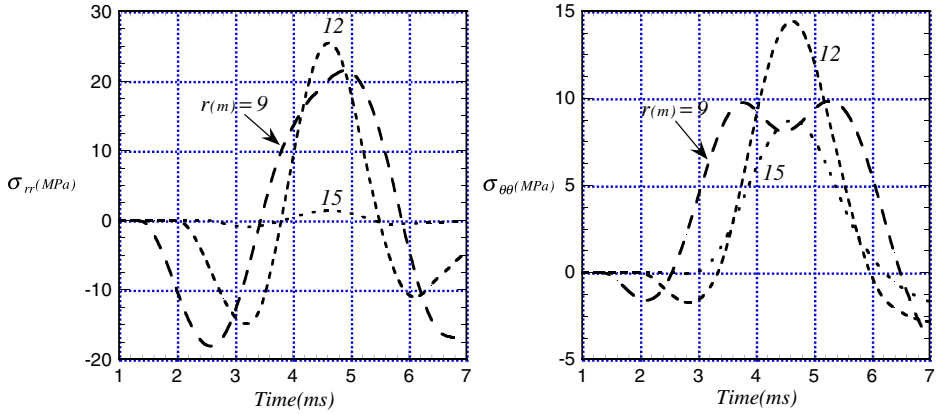

(a) Radial stress (b) Circumferential stress

Figure 6. Plots of stress as functions of time at the designated locations with the tunnel included using the one-dimensional code.

First, consider the radial stress plots shown in Figure 6(a). The stress at $r = 15$ m is approximately zero as it should be for a free surface. The plots for the other two locations should be compared with the free-field stresses shown in Figure 5(a). The initial compressive phases are identical with the corresponding free-wave profiles. However, the tensile phases display significantly larger amplitudes than the corresponding free-wave values. This phenomenon is a consequence of the compressive phase reflecting off the free (tunnel) surface as a tensile phase and combining with the original tensile tail. The result is an enhancement by nearly a factor of two in the peak tensile stress. The largest peak radial stress occurs near $r = 12$ m. As a consequence, it is expected that a region of cracks tangent to the free surface will appear in a region centered roughly 3 m to the left of the free surface.

With regard to the circumferential stress shown in Figure 6(b), the result is more complicated than one would expect of a pure reflection of the tensile part of the stress wave. The consequence is a potential for radial cracks to develop in the region adjacent to the free surface.

These one-dimensional numerical results of cylindrical wave propagation exhibit features that are not entirely intuitive. The potential for crack initiation develops as a consequence of the evolution of radial and circumferential stresses, and of interactions of reflection off a free surface of tensile and compressive phases of a wave. For a pulse with the magnitude and duration considered, both radial and circumferential cracks are expected adjacent to the source, and within a region of length at least 3 m adjacent to the front face of a tunnel free surface. We next examine the more realistic problem of two-dimensional features of wave reflection and refraction.

4.3. Two-dimensional elastic-wave solution with no tunnel

The MPM is used for the full two-dimensional study under the assumption of plane strain. MPM solves the two-dimensional analog of the momentum equation (33). The computational domain is shown in Figure 2a. The boundary condition on the cylinder is given by equation (1). The material external to the cylinder is granite, modeled by the material parameters given in Table I. The tunnel is a void in the domain with traction-free boundary conditions. The boundary conditions on the artificial square domain do not play a role because simulations are terminated before any reflections from these boundaries reach points of interest in the interior of the domain. The deformations in this problem are small, so MPM does not have a particular advantage over the finite element method. However, future simulations that might include larger deformations and falling rock could benefit from using MPM.

The results from the one-dimensional finite element code are used to choose a suitable element size for the two-dimensional code. Then, the two-dimensional code is used to provide illustrative results for the interaction of the stress wave with the tunnel, again under the assumption of elasticity, and with an eye toward implications for zones of damage when failure is included in the subsequent sections

DOI: 10.1002/nag

The elastic propagation of a pulse is investigated with a mesh of square elements of side length h, and four material points per element. The computational domain for the free-wave problem is shown in Figure 2(a) with details near the cylinder and points of interest shown in Figure 2(b). The numerical solutions are meaningful until a wave reflection occurs at the right boundary of the computational domain and the reflection front arrives at an observation point. The arrival time for a reflection front at a point with coordinate x_p is approximately $t_p = [52 + (55 - x_p)]/c_w$, which yields the following maximum times for which the solution is considered valid for observation points as shown in Figure 2(b): $(t_a, t_b, t_c, t_g, t_e) = (22, 21, 20, 19, 18)$ ms. Points a, b and c roughly correspond to $r = 3$, 6 and 9 m in Figure 2(b). Points g, e and f are close to the tunnel free surface and are of interest later when failure is included.

We begin the two-dimensional analysis with a convergence study and with code verification by comparison with the one-dimensional results. The equations of motion are solved in Cartesian coordinates so that the surface of the cylinder is also discretized with square elements and has a stair-step boundary. In order to illustrate the effect of using square elements for an axisymmetric problem and to demonstrate convergence with mesh refinement, results for the radial and circumferential components of stress at points a and b are shown in Figure 7. The shear component $\sigma_{r\theta}$ is zero because these two points lie on the horizontal axes ($\theta = 0$). The plots of σ_{rr} for $r = 3$ m in Figure 7(a) are essentially that of the applied pulse with a slight attenuation due to the fact that the stress point is at a radius slightly greater than 3 m. For the radial component of stress at $r = 3$ m, convergence is achieved for $h = 0.25$ m. For $\sigma_{\theta\theta}$, convergence is also achieved with the results being almost indistinguishable with $h = 0.125$ and 0.0625 m. At $r = 6$ m, convergence is achieved for $h = 0.25$ m for both stress components as indicated in Figure 7(b). In Figure 8, two-dimensional and

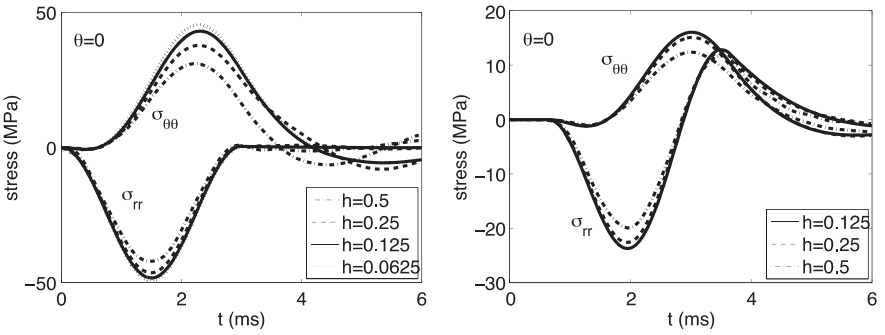

(a) Point a (r = 3m). (b) Point b (r = 6m)

Figure 7. Two-dimensional solutions with mesh refinement for radial and circumferential components of stress as functions of time.

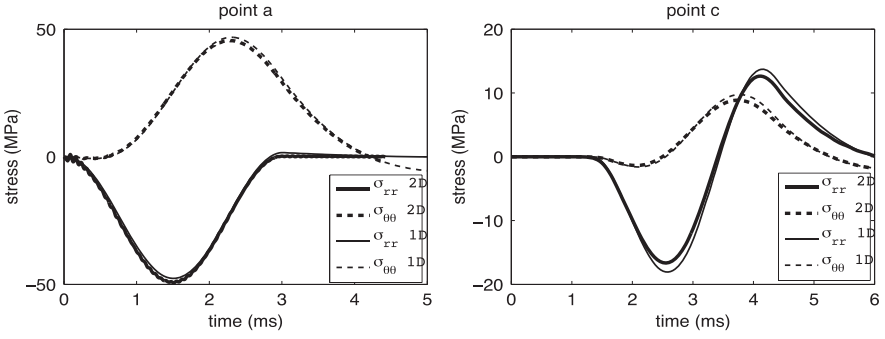

(a) Point a, (r = 3m). (b) Point c (r = 9m).

Figure 8. One-dimensional and two-dimensional numerical solutions of stress components as functions of time. (At point a, $\sigma_{\theta\theta}$ is calculated using $h = 0.0625$ m in two-dimensions.)

DOI: 10.1002/nag

one-dimensional results for stress as a function of time at points *a* and *c* are overlaid, showing good agreement.

To further illustrate the potential error of using a square mesh for axisymmetric wave propagation, we look at the predictions of stress as a function of time for points at radii of $r = 3$ m and $r = 6$ m, for three orientations ($\theta = 0,\ \pi/8,\ \pi/4$). The off-axis locations are indicated in Figure 2(b) with unlabeled points. The curves for the radial and circumferential components of stress at the three orientations are overlaid in separate plots for each radial position in Figure 9. We note that for points on the surface of the cylinder ($r = 3$ m) in Figure 9(a), there is some difference with orientation, whereas for an axisymmetric problem, there should be no difference. However, Figure 9 (b) shows that by the time the wave has propagated to $r = 6$ m, there is very little difference suggesting that for larger values of *r*, there is practically no distortion because of the use of a square mesh. We conclude from these studies that a mesh size of $h = 0.25$ m provides good accuracy for points of interest away from the cylindrical loading surface.

The failure model and the numerical simulations are based on the assumption that the *x*–*y* plane exhibits the maximum and minimum principal stresses. To determine the potential directions of maximum and minimum principal stresses, the three normal components of stress are plotted in Figure 10(a). These are principal stresses because the shear components are zero for a point on the *x*-axis. We note that the radial and circumferential stresses agree well with the one-dimensional results of Figure 5. The plot of maximum and minimum principal stresses in three dimensions is given in Figure 10(b), and the plot of maximum and minimum principal stresses for stress in the *x*–*y* plane is shown in Figure 10(c). There is some difference, but the critical observation is that the maxima and minima of these principal stresses over time are the same for both plots. A similar situation holds for all other points tested. Therefore, we assume that the maximum and minimum

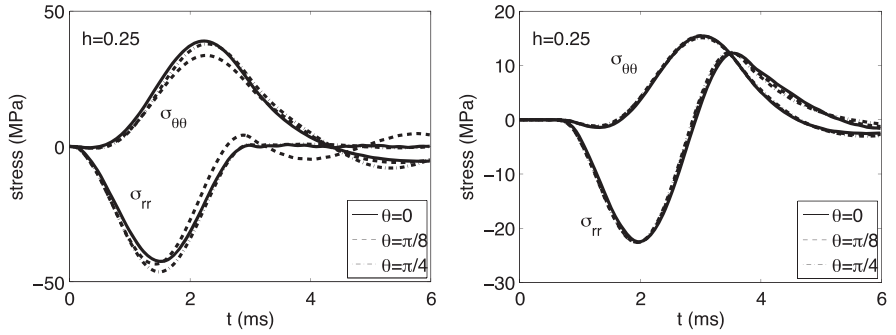

(a) $r = 3$m (b) $r = 6$m

Figure 9. Two-dimensional solutions for radial and circumferential components of stress as functions of time for two radii and three orientation angles.

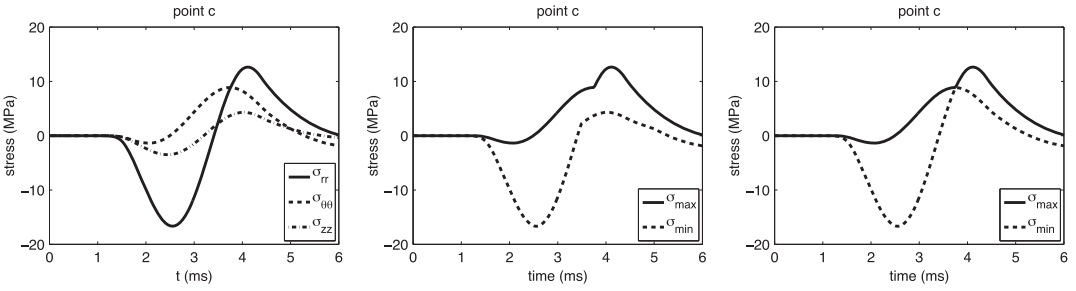

(a) Cylindrical components (b) Min and max components including σ_{zz} (c) Min and max components excluding σ_{zz}

Figure 10. Plots of components of stress (shear components are zero) as functions of time for point *c* ($r = 9$ m) for the free-field wave.

DOI: 10.1002/nag

stresses based on components in the x–y plane are appropriate for predicting failure and that plane strain continues to hold.

4.4. *Two-dimensional elastic-wave solutions with a tunnel*

Here, we consider elastic waves from the blast interacting with a tunnel. In this section, we concentrate our attention on observation point c. Detailed results at points near the tunnel are given in Section 5 for elastic solutions and solutions with failure. Reflections off the tunnel wall are an essential part of the analysis. The forward propagating wave from the blast reflects off the tunnel, and the front of the reflected wave reaches point c at approximately 4 ms. The wave reflected from the tunnel continues to propagate and reaches the cylinder surface, and a second reflection occurs. Because this second reflection should actually come from the damaged blast zone and we do not model the blast accurately, the solution reflected from the cylinder wall is not valid. The maximum time for solutions at a given observation point to be valid is approximately $t_m \approx [24 + \delta]/c_w$ in which δ denotes the distance (m) from point a to the observation point. For point c, this maximum time is $t_{cm} = 7$ ms.

For point c, the plots of the cylindrical components of stress and the maximum and minimum principal stresses are given in Figure 11(a) and 11(b), respectively. The shear component $\sigma_{r\theta}$ becomes slightly nonzero because of the break in axisymmetry due to the tunnel. In comparison with the one-dimensional solution for a free surface shown in Figure 6, the maximum value of the radial stress for the two-dimensional solution is reduced significantly, and the circumferential stress shows only one peak instead of two, although the peak values of circumferential stress are approximately the same. These differences are attributed to the interaction of the wave with the true tunnel shape rather than the idealized shape implied by the radial boundary condition in the one-dimensional solution.

The plots of Figure 11 can be compared with the free-field solution of Figure 10 to show the effect of reflection off the tunnel wall. Note that the two solutions shown in Figures 10 and 11 are identical until $t = 4$ ms, the arrival time of the reflected wave. The presence of the tunnel enhances the tensile phase of σ_{rr} because the reflection of the compressive part of the wave from the free surface (the tunnel wall) becomes tensile and interacts with the tensile tail. The appearance of large tensile radial stress presages the appearance of circumferential cracks. The maximum tensile value of $\sigma_{\theta\theta}$ remains unchanged from the free-field solution. Also, the same number of maxima and minima appears in Figures 10 and 11 for the free-field and reflected wave solutions.

These results of elastic-wave propagation for a free field and for the effects of a tunnel are included to emphasize the following points: (i) for the axisymmetric case, the two-dimensional results based on a rectangular grid are identical with the one-dimensional solutions; (ii) the evolution of radial and circumferential components of stress has significant implications concerning potential failure patterns; (iii) reflections can cause larger than expected enhancements of tensile stress because of interactions with tensile tails; and (iv) the maximum and minimum values of principal stress can be obtained using the in-plane components of stress.

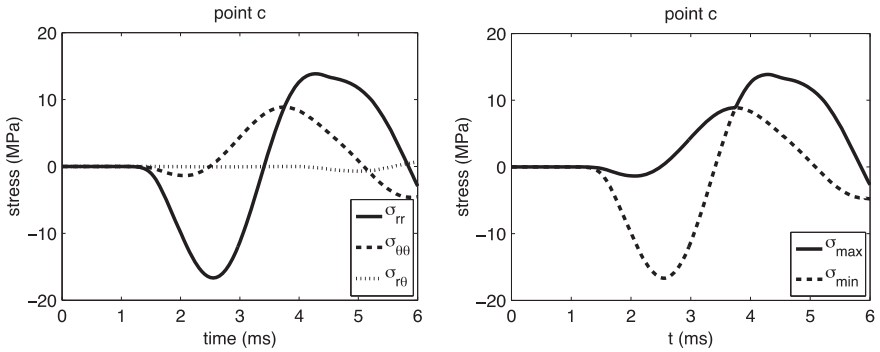

(a) Cylindrical (b) Max and min principal stresses

Figure 11. Plots of stress components as functions of time for point c ($r = 9$ m) with reflection off tunnel.

DOI: 10.1002/nag

4.5. *Fracture patterns without a tunnel*

Decohesion is added to the constitutive equation to obtain the effect of fracture with the first problem being one without the tunnel. In the following plots, cracks across an element are averaged results associated with the material points within the element. A crack is shown with a dark line tangent to the material failure surface only if $[u_n] \geq [u_0]$. Major cracks, defined by $[u_n] \geq 10[u_0]$, are shown with wider lines. A maximum of two cracks is allowed at each material point.

The evolution of the crack fields for three mesh sizes is shown in Figure 12 at time $t = 7$ ms. For all cases, the cracks extend to about 15 m from the origin, which is approximately the distance traveled by the maximum part of the compressive segment of the pulse. The combination of compressive radial stress with circumferential tensile stress, corresponding to the region B-C in Figure 4(b), indicates that radial cracking might be more extensive than if a pure Rankine criterion for failure was used. In addition, there is an indication of circumferential rings of cracks that can be attributed to the tensile tail of σ_{rr} in cylindrical geometry. If the magnitude of the forcing pulse was reduced sufficiently, then circumferential cracking would not occur.

Although the patterns look somewhat different, each plot shows the development of two primary sets of cracks, radial and circumferential. However, the finer mesh shows a richer structure, and the difference may be disconcerting. As has been noted [22, 23], standard convergence theory does not apply to discontinuous fields, and convergence with mesh refinement is an open question.

Principal stress components as functions of time for $h = 0.25$ m are given in Figure 13 for point c. Note that with the addition of decohesion, no tensile component of stress is larger than $\tau_{nf} = 5$ MPa, whereas with no failure, the maximum tensile stress is 12 MPa as shown in Figure 10(c). Another effect of decohesion is that the minimum stress is lower than that shown in Figure 10(c). Once

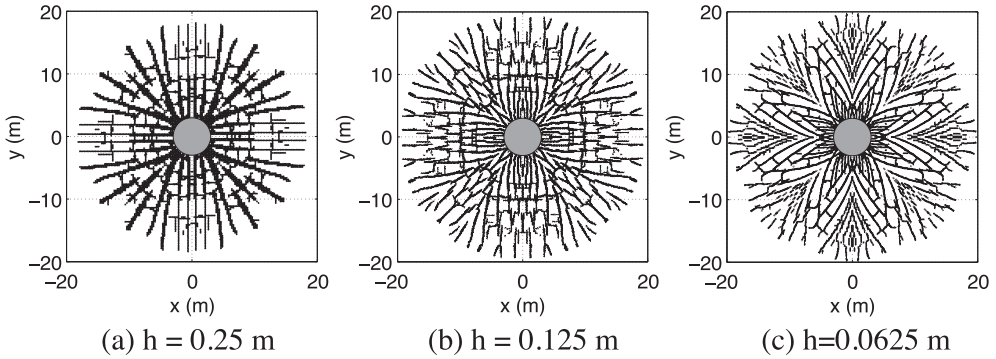

Figure 12. Crack patterns without tunnel at $t = 7$ ms for three mesh sizes.

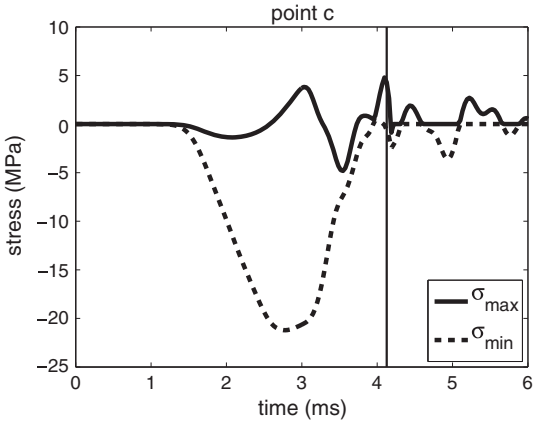

Figure 13. Stress components as functions of time at point c ($r = 9$ m) with $h = 0.25$ m for the case of no tunnel and decohesive failure. The vertical line indicates the initiation of the failure.

DOI: 10.1002/nag

decohesion occurs, axisymmetry is broken, so there is a small difference between the normal components ($\sigma_{rr}, \sigma_{\theta\theta}$) and the principal values ($\sigma_{\max}, \sigma_{\min}$) because $\sigma_{r\theta}$ (not shown) is slightly different from zero. Figure 13 shows a drop in stress at the time, $t = 3$ ms. However, this drop in stress is due to unloading from a radial crack (large circumferential stress) that occurs in an adjacent element. This stress drop is an example of the need for caution in interpreting stress plots. The vertical line in Figure 13 at $t = 4.2$ ms marks the initiation of a circumferential crack (tensile radial stress) that does occur at point *c*.

Next, we look at the effect of mesh refinement with plots of radial and circumferential stress in Figure 14 for three mesh sizes. The plots of radial stress and circumferential stress are identical until circumferential failure occurs at approximately $t = 4.2$ ms and the radial stress drops at $t = 3$ ms, respectively, after which results for the finer mesh display higher frequency oscillations. The plot of circumferential stress shows the effect of reflection off the cylindrical surface for t close to 8 ms.

4.6. Fracture patterns with a tunnel

When the tunnel is present, additional cracking will occur because of reflections off the tunnel wall. Of particular interest are failure patterns near the tunnel surface. At $t = 7$ ms, Figure 15 shows patterns for the two smaller mesh sizes while Figure 16 shows the pattern for the mesh size $h = 0.25$ m, the size used for subsequent results. Again, we see variations in the fracture patterns due to different mesh sizes, but there is a consistency with regard to the zones of failure near the front face and at points of particular interest along the tunnel wall. We discuss these points with specific reference to Figure 16.

General areas of failure near the tunnel include the region near the tunnel wall closest to the source, the lower left corner of the tunnel, a region on the top slightly beyond the transition from the straight to

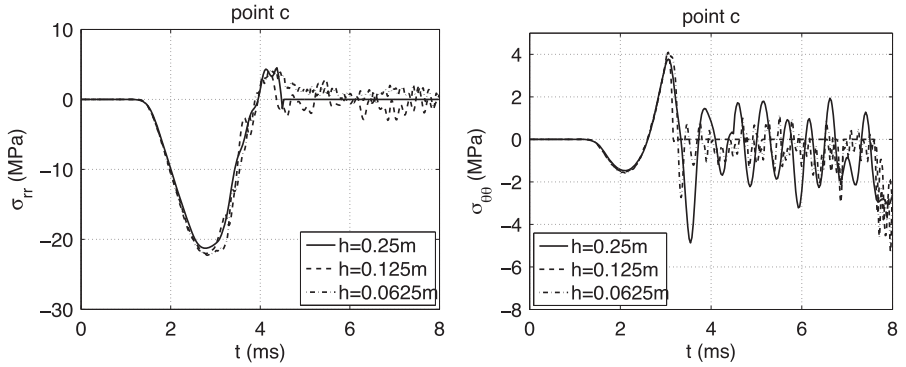

(a) Radial stress (b) Circumferential stress

Figure 14. Plots of radial and circumferential stress as functions of time for three mesh sizes.

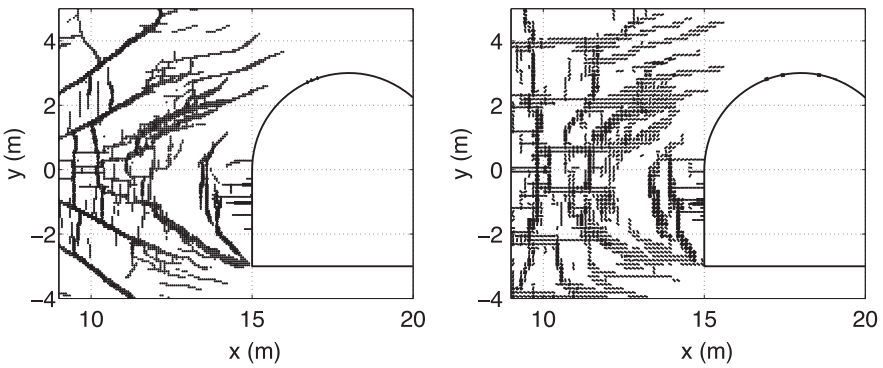

(a) $h = 0.0625$ m (b) $h = 0.125$ m

Figure 15. Failure patterns for regions next to the tunnel at $t = 7$ ms for the two smallest mesh sizes.

DOI: 10.1002/nag

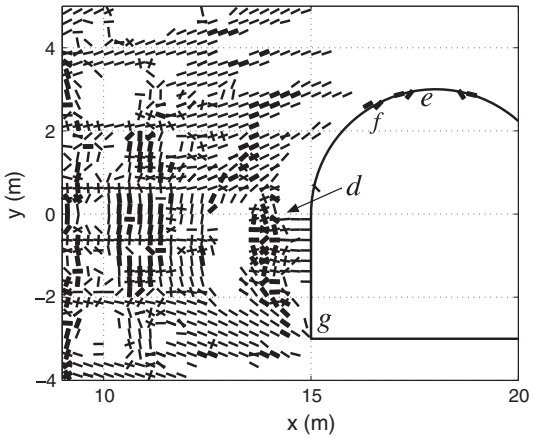

Figure 16. Crack distribution and orientation in the vicinity of the tunnel at $t = 7$ ms with $h = 0.25$ m where thin lines in the plot denote cracks with $[u_n] \geq [u_0]$ and thick lines denote $[u_n] \geq 10[u_0]$.

circular segments of the tunnel wall and points along the top of the tunnel. A series of horizontal cracks are developed along the front wall of the tunnel because of tensile values of circumferential stress. The radial component of stress is zero because of the free surface. When the initial compressive part of the radial pulse meets the free surface of the tunnel wall, it reflects as a tensile phase. Approximately 3 m to the left of the tunnel wall, a region with vertical cracks develops because of the combination of the tensile tail with the reflected compressive phase. The point *d* shown in Figures 2b and 16 is chosen to be within this zone. A small region to the left of these cracks is sheltered and exhibits few or no cracks.

Along the upper left portion of the tunnel roof, cracks tangent to the surface are displayed at points *e* and *f* in Figure 16. Because the normal component of traction is zero, these cracks are due to axial splitting. The result of such cracks at *e* and *f* will be spallation and would not be predicted by a Rankine failure criterion. If gravity were present, it is expected that these failed regions along the roof would fall to form rubble on the tunnel floor. In some cases, it appears that cracks have moved within the surface of the tunnel. This is a consequence of the numerical procedure where cracks are displayed at cell centers rather than at individual material points. The fracture at point *g* is due to biaxial compression. The next section provides a detailed analysis of the stress fields at these points and the influence of reflection and refraction, and the modes of failure on the stress evolution.

5. SPECIFIC FEATURES OF NUMERICAL SOLUTIONS WITH FAILURE

5.1. Preliminary comments

In Section 5.2, specific features of stress are shown at key points in the domain to illustrate significant observations. To demonstrate the complex interactions of cylindrical wave evolution, reflections and cracking, maximum and minimum principal values of stress as functions of time are analyzed for free-field elastic waves, elastic waves in the presence of the tunnel, free-field elastic-decohesive waves, and reflected, elastic-decohesive waves. We focus on four points on the edge or near the edge of the tunnel at which cracking occurs as identified by the fracture plots of the previous section. These points are labeled *d*, *e*, *f* and *g* in Figure 2(b). Specifically, with *h* denoting the side length of an element, the coordinates of these points are $(13.5 + h/4,\ h/4)$,$(18 + h/4, 3 + h/4)$, $(16 - h/4,\ 2.5 + 3h/4)$ and $(15 - h/4, -3 + h/4)$ m respectively. As noted in Section 4.4, the maximum time for solutions at a given observation point to be valid is approximately $t_m \approx [24 + \delta]/c_w$ in which δ denotes the distance from point *a* to the observation point. For the observation points (*d*, *e*, *f*, *g*), these maximum times are approximately $(t_{dm}, t_{em}, t_{fm}, t_{gm}) = (8, 9, 8.6, 8)$ ms. It is seen that these times are less than those governed by reflections from the computational boundary. Because the maximum values of stress occur before these maximum times, the following plots of stress are terminated at $t = 8$ ms.

DOI: 10.1002/nag

A small parameter study on the effect of pulse duration is provided in Section 5.3. The first set of problems is identified by the symbol $S(t_D$ ms) in which S denotes the side-on configuration shown in Figure 2(b) and t_D is the duration of the pulse. In Section 5.4, a rotated tunnel configuration is considered, and these problems are identified as $R(t_D$ ms). In all cases, the minimum distance between the surfaces of the cylinder and the tunnel is 12 m. Section 5.5 discusses the energetics of the failure process for the representative problem S(3 ms).

5.2. *Solutions for problem* S(3 ms)

First, we discuss the solutions for point d. The results are given in Figure 17. For the purely elastic case, the effect of reflection shown in Figure 17(b) shows significant enhancement in the magnitude of tensile stress of the free-field stress given in Figure 17(a). Note in Figure 17(b) that it is possible for the maximum and minimum principal stresses to be positive at the same time. Now compare the free-field elastic solution with the free-field elastic-decohesion solution of Figure 17(c). The maximum stress is now limited by the tensile failure stress, τ_{nf}, and the minimum stress has been enhanced. The change in the free-field stress with decohesion is a consequence of significant cracking closer to the source and not just of cracking at point d. In the presence of the tunnel, Figure 17(d) shows the formation of two cracks at times indicated by the two vertical lines. These cracks have different orientations and are caused primarily by the tensile circumferential stress. The ability to capture more than one failure plane at a given point in a robust manner is an important attribute of the decohesive approach.

For the remaining points, we omit the free-field elastic and elastic-decohesion results because the differences from those presented in Figure 17(a) and 17(c) are minor and due only to the decay and evolution resulting from being further from the source. We continue to show the elastic results with a tunnel because the complex evolution of waves around the tunnel provides insight to the development of stresses that cause failure.

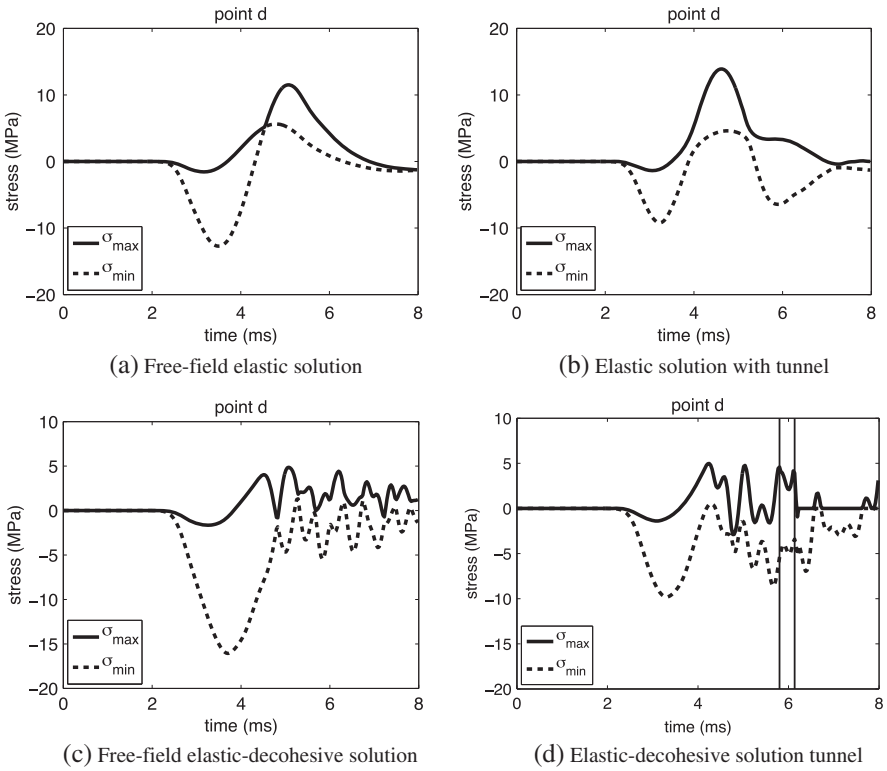

(a) Free-field elastic solution (b) Elastic solution with tunnel

(c) Free-field elastic-decohesive solution (d) Elastic-decohesive solution tunnel

Figure 17. Maximum and minimum stresses as functions of time at point d. The vertical lines indicate the initiation of the failure.

DOI: 10.1002/nag

Figure 18 shows results for point *e* on the top surface of the tunnel. The elastic wave with the tunnel has changed considerably from the free-field solution with Figure 18(a) showing a significant enhancement of the minimum stress. Surprisingly, if failure is allowed, there is further enhancement of the minimum principal stress as shown in Figure 18(b). However, the magnitude of the stress is not large enough to cause axial splitting.

The situation is different at point *f* as indicated by the time histories shown in Figure 19. The stress point that is monitored is within the rock slightly away from the tunnel surface. At this location, a small tensile stress develops, and in conjunction with a significant compressive stress in a direction tangent to the tunnel surface, cracking is predicted. The moment of initial cracking is identified with the sudden drop in the tensile stress and occurs at the time indicated by the vertical line in Figure 19(b). The combination of one tensile principal stress with a negative principal stress exists on segment B-C of the failure surface of Figure 4(b). Thus, the failure at point *f* is close to axial splitting.

Finally, we show the results in Figure 20 for point *g* located at the lower left corner of the tunnel. With the elastic solution shown in Figure 20(a), we see a large enhancement of both the maximum and minimum principal stresses. On the other hand, when failure is allowed, both principal stresses exhibit surprisingly large decreases in the minimum principal stress and become negative, as indicated in Figure 20(b). The vertical line in Figure 20(b) shows when failure first occurs as governed by segment C-D in the failure surface of Figure 4. The continued decrease in the minimum principal stress suggests the possibility of additional failure. However, the maximum principal stress also decreases slightly, and the failure surface of Figure 4 indicates that the value of the minimum principal stress for failure decreases rapidly so that additional failure does not occur.

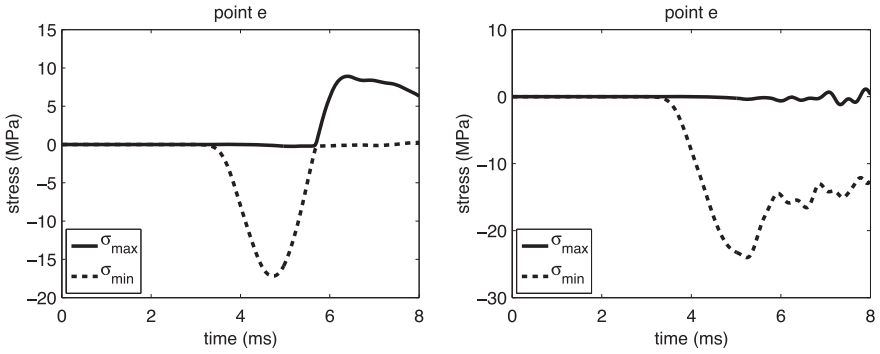

(a) Elastic solution. (b) Elastic-decohesive solution.

Figure 18. Maximum and minimum stresses with tunnel as functions of time at point *e*.

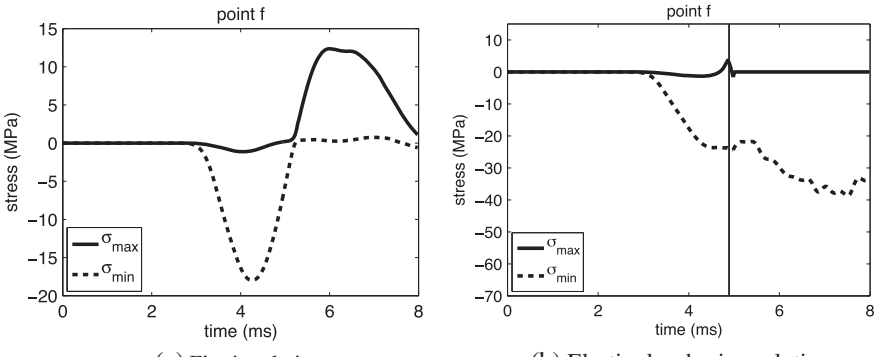

(a) Elastic solution. (b) Elastic-decohesive solution.

Figure 19. Maximum and minimum stresses with tunnel as functions of time at point *f*. The vertical line indicates the initiation of the failure.

DOI: 10.1002/nag

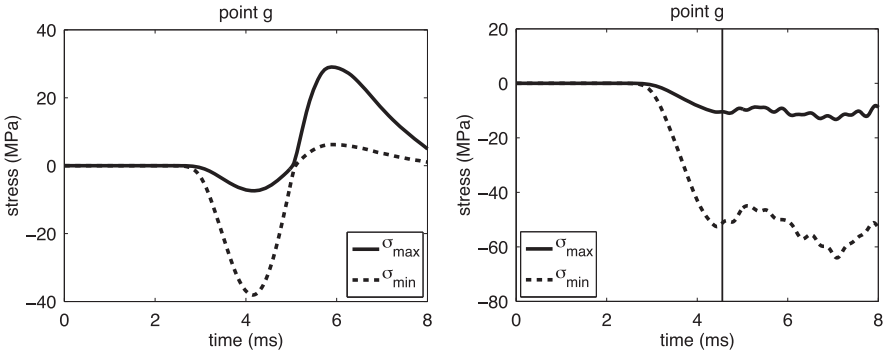

(a) Elastic solution. (b) Elastic-decohesive solution.

Figure 20. Maximum and minimum stresses with tunnel as functions of time at point g. The vertical line indicates the initiation of the failure.

The failure at point g occurs as a result of a biaxial compressive state, and considerable damage can be expected in the vicinity of this point.

5.3. *Solutions for problems* $S(1.5\,\text{ms})$ and $S(6\,\text{ms})$

Here, we look at the effect of shortening and lengthening the duration of the loading pulse to $t_D = 1.5$ ms and $t_D = 6$ ms , respectively. Increasing the duration results in a proportional increase in both the impulse and the energy imparted by the boundary condition. When decohesion is allowed, Figure 21 provides plots of crack distributions and orientations at a time of $t = 7$ ms. The shorter pulse provides much more cracking adjacent to the front face of the tunnel in comparison with the pulse with a longer duration. The reason is that for a shorter pulse, the effective wavelength of the compressive radial phase of the stress wave is also shorter. The peak of the reflected tensile wave occurs at approximately half the wavelength and, hence, is closer to the face of the tunnel. Even though the energy is less, the result of a more impulsive (short duration) pulse results in considerably more cracking in the vicinity of the tunnel.

Figure 22 shows the stress as functions of time at points d, f and g for the two pulse durations. Both Figures 21 and 22 suggest tensile circumferential failure at point d. The vertical lines in each frame of Figure 22 for point d indicate the initiation of failure for each pulse duration. The shorter pulse duration shows a second drop in stress around $t = 6$ ms, but this drop is due to unloading from a crack in an adjacent element.

The situation at point f shown in Figure 22 is quite similar to Figure 19(b) where a small tensile maximum principle stress combines with large compressive minimum principal stress resulting in

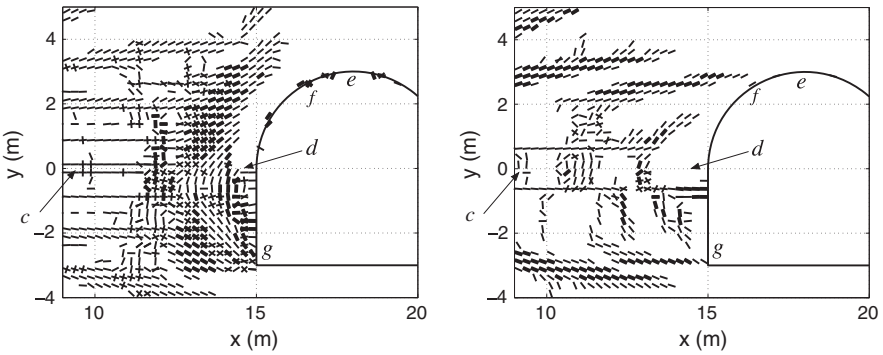

(a) $t_D = 1.5$ ms (b) $t_D = 6$ ms

Figure 21. Crack distribution and orientation in the vicinity of the tunnel at $t = 7$ ms where thin lines in the plot denote cracks for $[u_n] \geq [u_0]$ and thick lines denote $[u_n] \geq 10[u_0]$.

DOI: 10.1002/nag

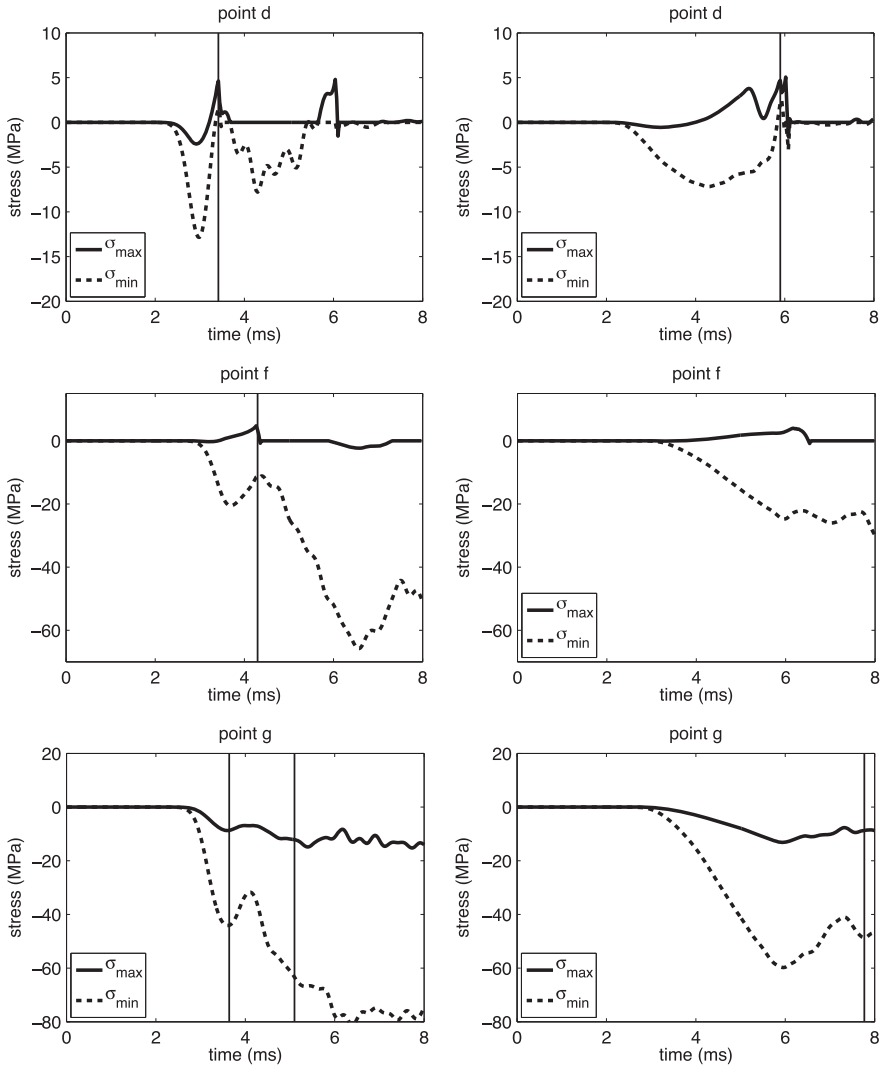

(a) $t_D = 1.5$ ms (b) $t_D = 6$ ms

Figure 22. Maximum and minimum stress components as functions of time with the tunnel and decohesion for several points and for two pulse durations. The vertical lines indicate the initiation of the failure.

nearly axial splitting. For the forcing pulse of shorter duration and at a later time, the compressive stress decreases below $-f_c^{'}$ so that additional axial splitting occurs. The splitting occurs at a later time for the longer pulse duration. For point *g* (lower left corner), cracking occurs for both pulse lengths, but for the shorter pulse duration, there is a much greater enhancement of the minimum compressive stress after an initial failure surface is formed, and two cracks appear with different orientations, but both due to biaxial compression. A similar crack appears at a later time for the longer pulse duration.

The salient observation is that the reflected pulse from the tunnel free surface causes significantly more damage closer to the tunnel as the pulse duration is shortened with the magnitude held constant.

5.4. Solutions for problems R(1.5 ms) and *R*(3 ms)

Finally, we consider a configuration, which, in the absence of gravity and with a 90° rotation, represents a blast load directly above the tunnel. If decohesion is allowed, the crack pattern and crack orientations for this rotated geometry are given in Figure 23 for two pulse durations. Now we see that the fracture pattern is almost symmetric about the *x*–*z* plane with tunnel failures in the

DOI: 10.1002/nag

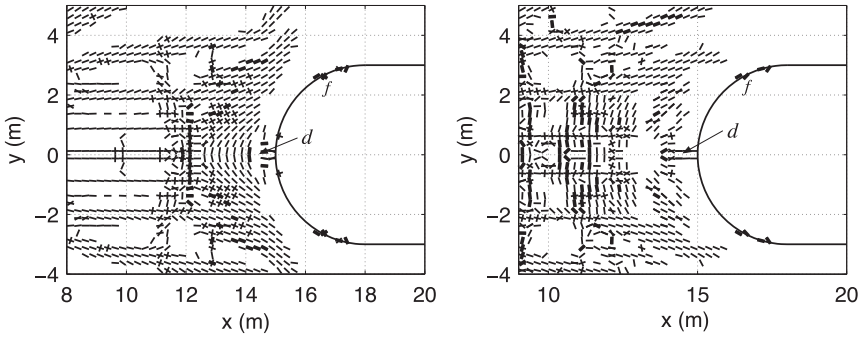

(a) $t_D = 1.5$ ms (b) $t_D = 3$ ms

Figure 23. Crack distribution and orientation in the vicinity of the tunnel at $t = 7$ ms for two durations of time where thin lines in the plot denote cracks with $[u_n] \geq [u_0]$ and thick lines denote $[u_n] \geq 10[u_0]$.

region closest to the source and at points on the circular segment of the tunnel roughly where lines through the origin intersect the tunnel tangentially. There are radial cracks at the tunnel apex, and vertical cracks at a short distance to the left of the apex, with a sheltered, crack-free region in between. The vertical cracks are closer to the tunnel for the pulse of shorter duration. These general features are also observed with the previous orientation.

Stress components as functions of time are shown for points d and f in Figure 24. These results are analogous to those for the corresponding points in the original configuration shown in Figure 22(a) for $t_D = 1.5$ ms, and Figures 17(d) and 19(b) for $t_D = 3$ ms. With this current configuration, there is no corner to provide an additional region of potentially significant damage.

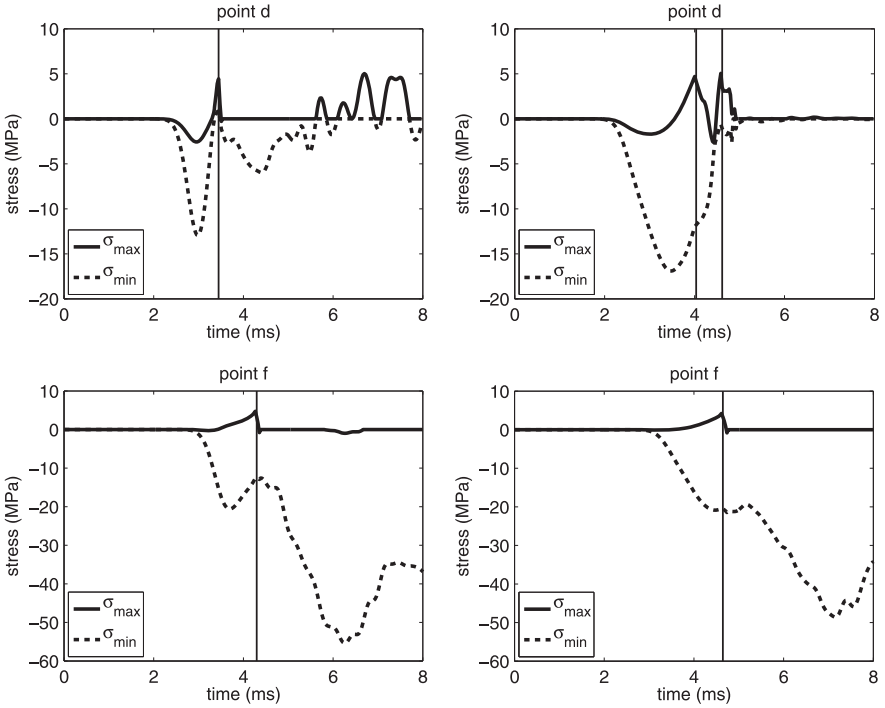

(a) $t_D = 1.5$ ms (b) $t_D = 3$ ms

Figure 24. Maximum and minimum stress components as functions of time for points d and f with decohesion for two pulse durations with blast above tunnel. The vertical lines indicate the initiation of the failure.

DOI: 10.1002/nag

5.5. Energetics

When one looks at the fracture fields, a natural question is how much work is used to form the cracks. Figure 25 summarizes the energetic aspects of the failure process for one of our simulations. Specifically, the graphs summarize the energy components as functions of time for the tunnel configuration sketched in Figure 1, with a pulse duration of 3 ms and a mesh size of $h = 0.25$ m. The failure process for this case is discussed in Sections 4.6 and 5.2.

The work applied to the system as a function of time is

$$W(t) = 2\pi r_0 \int_0^t \sigma_{rr}(t) v dt \tag{34}$$

in which v is the radial velocity at the cylinder wall and $\sigma_{rr}(t)$ is the prescribed traction at the cylinder wall given in equation (1). The wall is located at $r_0 = 3$ m. Because we use a jagged representation of the cylinder boundary, this input energy per unit area is estimated by using the computed energy in one element of the simulation and multiplying by $2\pi r_0$, assuming symmetry. The failure energy, $W_F(t)$, is given in equation (17). It is computed by summing the contribution from each material point in the domain. For comparison, the figure also shows the total kinetic energy, $K(t)$, and total strain energy, $S(t)$, as functions of time. These energy components are also computed by summing over the material-point contributions. The failure energy is an order of magnitude smaller than the input energy. Thus, there is more than enough energy supplied to the system to cause the observed and continued fracturing. For this example, the failure energy is still increasing at $t = 8$ ms. If the input energy is lowered by decreasing σ_0 in (1), the failure energy reaches a maximum and remains constant thereafter.

6. SUMMARY

This study attempts to isolate the key features that would help determine the susceptibility of a tunnel to failure due to a blast. Several simplifying assumptions are made with the most important ones being: (i) the problem is reduced to plane strain through the use of a cylindrical charge with axis parallel to the tunnel, and (ii) the explosive pressure–time relation is replaced by a single compressive pulse. The great advantage of the latter assumption is that elastic wave propagation can be used to identify crucial attributes of waves in cylindrical geometry and their reflections off a free surface. One property of reflected waves is that the tensile part of the component of stress tangential to the free surface is enhanced. A second property is that the compressive part of the stress normal to the free

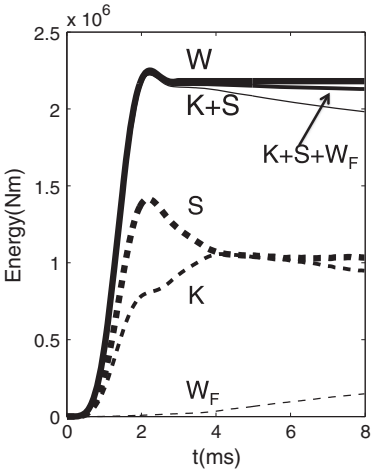

Figure 25. Plots of energy as a function of time.

DOI: 10.1002/nag

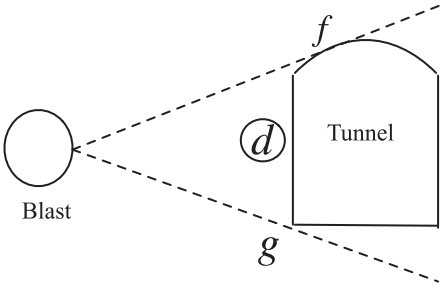

Figure 26. Sketch of points near a tunnel most likely to be damaged.

surface reflects as a tensile wave and reinforces the tensile tail. Both properties provide the potential for crack initiation if the enhancement is large enough.

There appear to be three major zones of significant cracking in the vicinity of a tunnel. These areas are shown in Figure 26. The first region, identified as *d*, contains cracks that are formed as a consequence of the properties near the free surface described earlier. The tensile stress parallel to the tunnel wall forms cracks that extend perpendicularly from the tunnel wall. The left side of this cracked region also contains cracks parallel to the tunnel wall, and these cracks are formed by the tensile normal stress perpendicular to the tunnel wall. These parallel cracks form at a distance from the tunnel wall that roughly corresponds to the wavelength determined by the duration of the loading pulse. For loading pulses with shorter durations, the region can extend down to the corner identified as *g*. The cracks in this region may not cause the failure of a tunnel wall, but it would be a region of considerable weakness for any subsequent blast load.

The other two regions are roughly at the tangent points, *f* and *g*, formed by rays drawn from the closest point of the blast surface. If point *f* lies on the surface of the tunnel, the in-plane stress must be a normal component tangent to the surface. This stress is generally negative and large and therefore can be a source of axial splitting. If point *f* lies slightly away from the surface, a small tensile principal stress normal to the surface can develop. The combination of the two principal stresses can cause failure at a value of the compressive stress smaller than the value required for axial splitting.

The region identified by the point *g* experiences biaxial compression with a relatively large value for the minimum principal stress. One source of stress enhancement at the corner is the interaction of the elastic wave with the corner. However, and somewhat surprisingly, there is a further enhancement when fracture is allowed to occur (and also for point *f*). Because of the effective change in constitutive properties, this enhancement might be due to refraction. Based on the failure surface shown in Figure 4(b), the failure in biaxial compression is mixed mode. Not surprisingly, considerable damage can be expected in the vicinity of the corner.

The use of the MPM with decohesive failure provides the means for obtaining an overall picture of material failure in the vicinity of a tunnel due to an impulsive load at some distance from the tunnel. A significant aspect of the numerical approach is the capability to predict more than one fracture in any element. Figure 26 provides a quick engineering indication of which zones might be most vulnerable. One point worth emphasizing is that the use of a simpler failure model, such as the Rankine maximum principal stress criterion, would not predict failure at points *f* and *g*. An important additional benefit of the proposed approach is that the decohesive history parameters are stored, so that after one loading event, the damaged state is known and can be used as an initial condition for numerical analysis of a subsequent disturbance.

ACKNOWLEDGEMENTS

This work was partially supported by Task Order #26 under Defense Threat Reduction Agency contract 01-03-D-0009 with the University of New Mexico. Discussions related to various aspects of this project with S. Babcock, D. Chitty and P. Randles were extremely helpful and greatly appreciated.

DOI: 10.1002/nag

REFERENCES

1. Yang Z. Finite element simulation to response of buried shelters to blast loading. *Finite Elements in Analysis and Design* 1997; **24**:113–132.
2. Ortiz M, Pandolfi A. A variational cam-clay theory of plasticity. *Computer Methods in Applied Mechanics and Engineering* 2004; **193**:2645–2666.
3. Wang Z, Lu Y, Hao H, Chong K. A full coupled numerical analysis approach for buried structures subjected to subsurface blast. *Computers and Structures* 2005; **83**:339–356.
4. Wang Z, Hao H, Lu Y. A three-phase soil model for simulating stress wave propagation due to blast loading. *International Journal for Numerical and Analytical Methods in Geomechanics* 2004; **28**:33–56.
5. Riedel W, Thoma K, Hiermaier S. Numerical analysis using a new macroscopic concrete model for hydrocodes. *In*: *Proceedings of 9th International Symposium on Interaction of the Effects of Munitions with Structures*, 1999; 315–22.
6. Hao H, Wu C, Zhou Y. Numerical analysis of blast-induced stress waves in a rock mass with anisotropic continuum damage models part 1: equivalent material property approach. *Rock Mechanics and Rock Engineering* 2002a; **35**(2):79–94.
7. Hao H, Wu C, Seah CC. Numerical analysis of blast-induced stress waves in a rock mass with anisotropic continuum damage models part 2: stochastic approach. *Rock Mechanics and Rock Engineering* 2002b; **35**(2):95–108.
8. Wu C, Lu Y, Hao H. Numerical prediction of blast-induced stress wave from large-scale underground explosion. *International Journal for Numerical and Analytical Methods in Geomechanics* 2004; **28**:93–109.
9. Wu C, Hao H. Numerical study of characteristics of underground blast induced surface ground motion and their effect on above-ground structures. Part I. Ground motion characteristics. *Soil Dynamics and Earthquake Engineering* 2005; **25**:27–38.
10. Wu C, Hao H. Numerical prediction of rock mass damage due to accidental explosions in an underground ammunition storage chamber. *Shock Waves* 2006; **15**(1):43–54.
11. Schreyer HL, Sulsky DL, Munday LB, Coon MD, Kwok R. Elastic-decohesive constitutive model for sea ice. *Journal of Geophysical Research* 2006; 111:C11S26. DOI: 10.1029/2005JC003334.
12. Sulsky D, Schreyer H, Peterson K, Kwok R, Coon M. Using the material-point method to model sea ice dynamics. *Journal of Geophysical Research* 2007; 112:C02S90. DOI: 10.1029/2005JC003329.
13. Sulsky D, Peterson K. Towards a new elastic-decohesive model of Arctic sea ice. *Physica D* 2012. DOI:10.1016/j.physletb.2003.10.071.
14. Banakaki M, Mohanty B. Numerical simulation of stress wave induced fractures in rock. *International Journal of Impact Engineering* 2012; **40-41**:16–25.
15. Zhu Z, Mohanty B, Xie H. Numerical investigation of blasting-induced crack initiation and propagation in rocks. *International Journal of Rock Mechanics and Mining Sciences* 2007; **44**:412–424.
16. Ma GW, An XM. Numerical simulation of blasting-induced rock fractures. *International Journal of Rock Mechanics and Mining Sciences* 2008; **45**:966–975.
17. Hamiel Y, Lyakhovsky V, Stanchits S, Dresen G, Ben-Zion Y. Brittle deformation and damage-induced seismic wave anisotropy in rocks. *Geophysical Journal International* 2009; **178**:901–909.
18. Khan GN. Discrete element modeling of rock failure dynamics. *Journal of Mining Science* 2012; **48**(1):96–102.
19. Kupfer HB, Gerstle KG. Behavior of concrete under biaxial stresses. *Journal of Engineering Mechanics* 1973; **99**(EM4):853–866.
20. Rutland CA, Wang ML. The effects of confinement on the failure orientation in cementitious materials: experimental observations. *Cement and Concrete Composites* 1997; **19**:149–160.
21. Schreyer HL. Modelling surface orientation and stress at failure of concrete and geological materials. *International Journal for Numerical and Analytical Methods in Geomechanics* 2007; **31**:141–171.
22. Cervera M, Chiumeti M, Codina R. Mesh objective modeling of cracks using continuous linear strain and displacement interpolations. *International Journal for Numerical Methods in Engineering* 2011; **87**:962–987.
23. Sulsky D, Schreyer H. MPM simulation of dynamic material failure with a decohesive constitutive model. *European Journal of Mechanics A/Solids* 2004; **23**:423–445.

DOI: 10.1002/nag